SUPPLEMENTARY INFORMATION for

CAST ALUMINIUM SINGLE CRYSTALS CROSS THE THRESHOLD FROM BULK TO SIZE-DEPENDENT STOCHASTIC PLASTICITY

J. Krebs*, S.I. Rao**, S. Verheyden, C. Miko, R. Goodall, W.A. Curtin and A. Mortensen

*Corresponding author for experiments, ** Corresponding author for simulations

Ecole Polytechnique Fédérale de Lausanne (EPFL); Lausanne CH-1015 Switzerland

Contents

1   Microcasting and wire retrieval processes

Prior to infiltration with molten aluminium of shaped cavities within the single-crystalline NaCl moulds, the entrance and the exit sides of the cavity going through the mould are marked with ink, Fig. S-1(a). Then, on the four other sides of the mould, sheets of 0.127 mm thick graphite foil (Ucar Carbon Company) slightly larger in area than the crystal sides are glued with carbon glue (Leit-C), Fig. S-1(c-e). Those carbon foil sheets serve as markers when retrieving the NaCl crystals from the cast ingot after infiltration. Two or three moulds (depending on their size) are then placed into an alumina crucible, previously coated with graphite spray (Kontakt Chemie Graphit 33 spray). Small (table salt) NaCl grains are poured around the moulds in order to hold them in the crucible with their opened sides (crystal faces without graphic foil) oriented approximately along the horizontal. Above the small salt grains, coarser (cooking) salt grains are added so that they break and filter off the aluminium oxide layer that covers the molten ingot. Finally, an ingot of 99.99% aluminium (Hydro Aluminium GmbH, Grevenbroich, Germany) is placed atop the ensemble, as illustrated in Fig. S-1(f). The infiltration chamber, half of which is sketched in Fig. S-1(g), can contain up to four crucibles. It is composed of three stainless steel parts connected by greased threads. Carbon foil rings are placed between the top and middle parts as well as along the bottom and middle parts to ensure airtightness (see Fig. S-1g). In addition, a 2 mm insulating alumina wool layer is placed inside the cylinder against its wall for thermal isolation. The top part, through which a thermocouple passes to measure the instantaneous temperature in the chamber, can be connected via a connector valve either to a vacuum pump or a 4N argon gas bottle. Once the chamber containing the crucibles is sealed and evacuated (0.5 mbar residual pressure), it is slowly lowered by means of a pulley into a resistance furnace pre-heated to 710°C. After roughly 45 min (30 min to heat up the crucibles at the furnace temperature plus 15 min to be sure that the ingots are entirely molten), the connector valve is switched to the gas pipe and 4N argon at 15 bar (1.5 MPa) is let into the chamber to push the molten aluminium into microcavities within the moulds. After a 3 minute hold time, the chamber is

taken out the furnace and placed onto a copper chill cooled by air flow pipes, to promote directional solidification of the metal. Figure S-2 sketches the thermal cycle during the infiltration process with drawings of what physically occurs at each step of the infiltration.
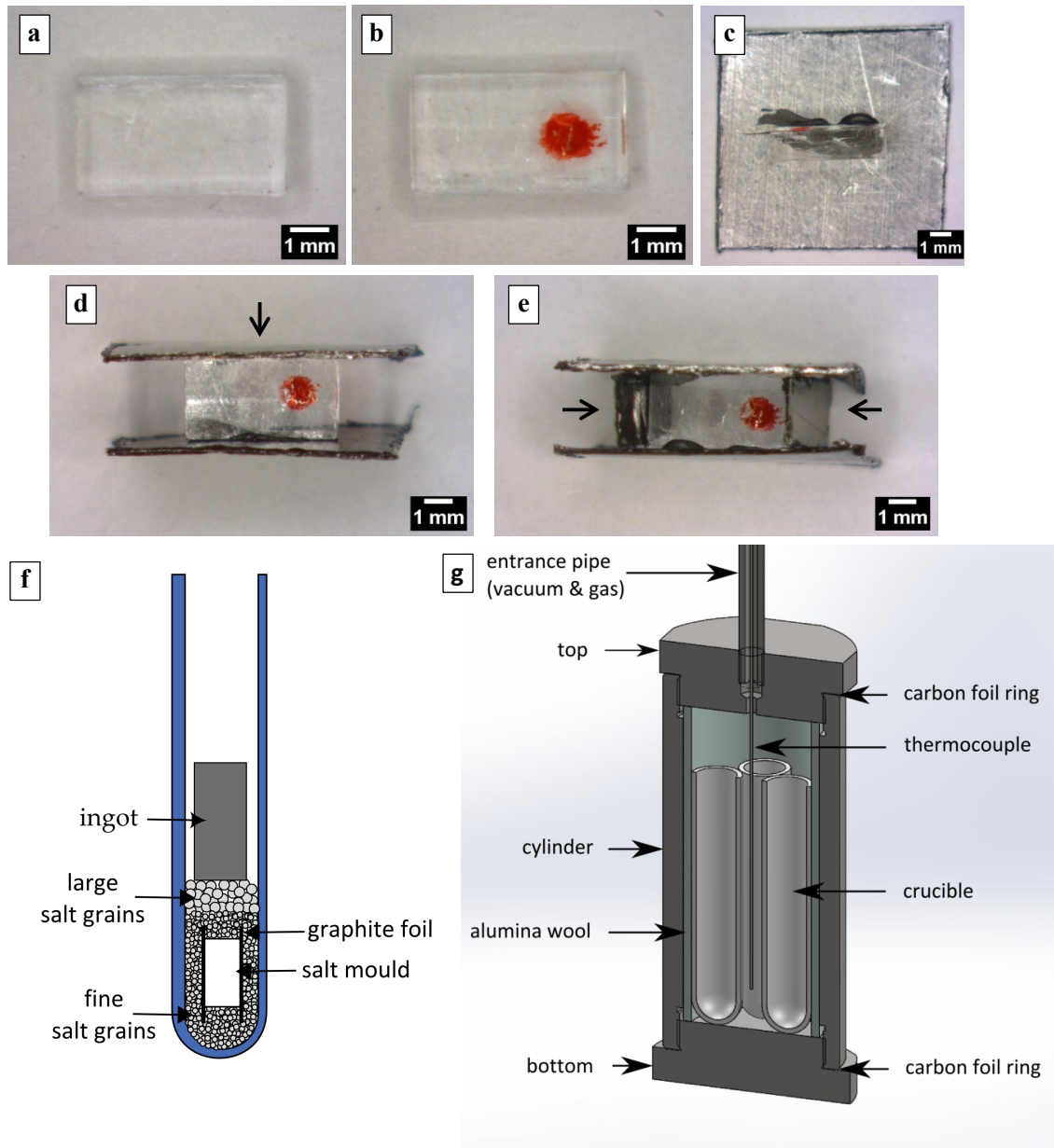
Figure S-1 – Producing the microcast wires. A cleaved mould (the cavity is too small to be visible in the image) (**a**); same marked with red ink to indicate sides along which the cavity emerges (**b**). On the four other sides of the moulds, graphite foils wider than the mould are attached using carbon glue (**c-e**). The mould assembly is then placed in an alumina crucible, surrounded with fine table salt, and then topped with coarse salt grains and an ingot of aluminium (**f**) before insertion in the pressure infiltration chamber (**g**).

Figure S-2 - Sketch showing the temperature cycle during the infiltration process with related illustrations of what physically occurs at each step of the infiltration. More information is given in the text.
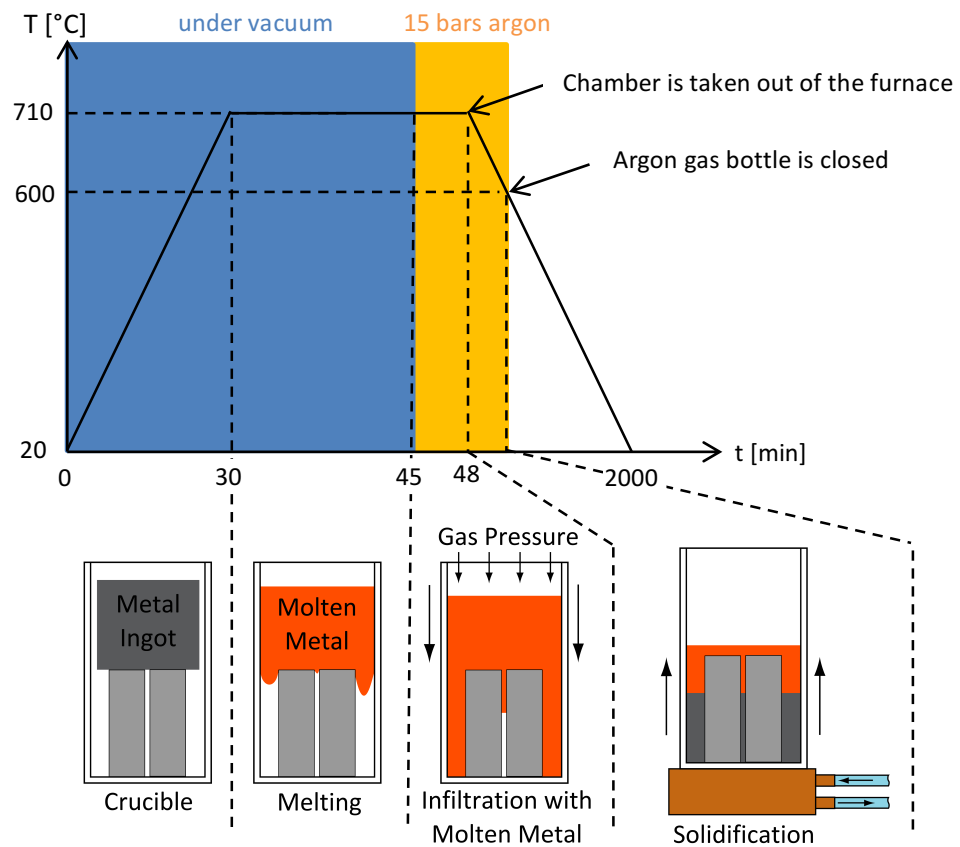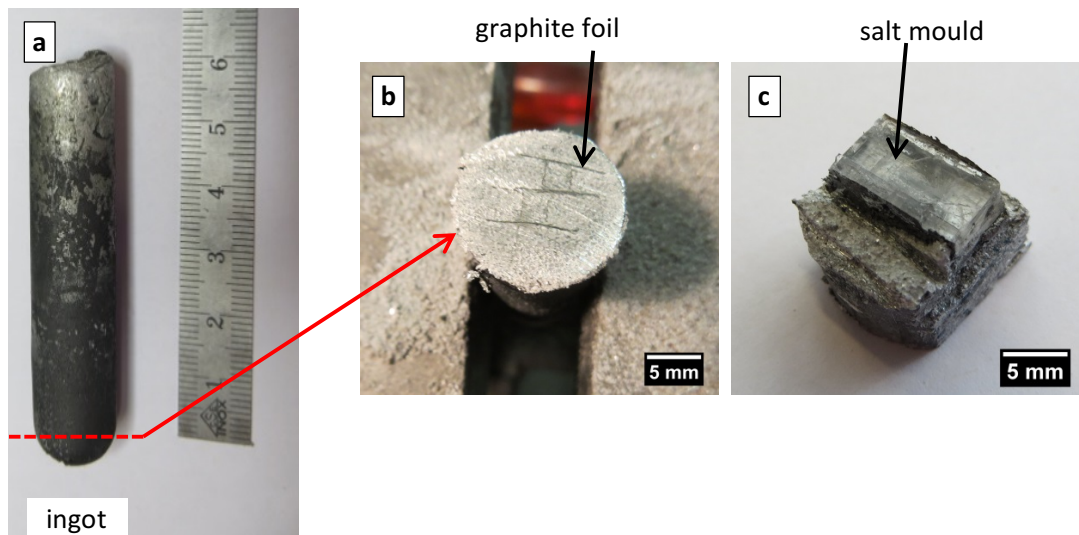

Figure S-3 - Photographs showing retrieval of the microcastings from their mould. Ingot after infiltration (**a**). The salt mould is contained within this ingot, near its rounded bottom. To extract the salt mould, the bottom of the ingot is sawed and filed to reveal the graphite foil parts (**b**); then the surrounding metal is removed by cutting, first along the graphite foils and then along remaining aluminium-salt interfaces (**c**).

Once cooled, the ingots are removed from their crucible Fig. S-3(a), cut near their bottom with a saw

and ground with a file until the graphite foils become visible, Fig. S-3(b). The salt moulds are then

4

removed from their ingots with a knife by cutting along the graphite foils, and then by cutting along the aluminium-salt interface for the two crystal sides without graphite foil, Fig. S-3(c). At this point, the salt moulds are free and their faces are carefully cleaned from carbon glue and aluminium residue by slight polishing on abrasive paper.

The microcastings are released by gently leaching the salt moulds in water containing a corrosion inhibitor, namely distilled water containing 0.84 g/l of $NaHCO_3$ and 1.62 g/l of Na_2CrO_4, corresponding to 0.01 mol concentrations of both $NaHCO_3$ and Na_2CrO_4. The dissolution set-up is composed of a side-arm glass Erlenmeyer, onto which a 0.2 μm alumina filter (Whatman Anodisc™) is placed over a support. The circular filter is held along its border by the wall of the tower and in its centre with a weight. Moulds are first dipped a couple of seconds into a small amount of chromate solution in order to remove the thinner residues on their surface. They are subsequently placed on the filter. Water solution is poured into the tower and finally ethanol is added over the water solution. Since ethanol has a lower density, it forms a layer resting atop the (quiescent) water. After roughly 30 min, the salt mould is dissolved and the vacuum pump is turned on, causing the water solution to be pulled through the filter followed by the ethanol layer, which serves two purposes: (i) cleaning the castings from the water solution and (ii) due to is low surface tension (σ_s = 22 mJ/m^2 for ethanol versus σ_s = 72 mJ/m^2 for water, *CRC Handbook of chemistry and physics*, 2015), capillary forces caused by ethanol meniscuses are less likely to deform the (fragile) microcastings upon drying. Finally, the filter on its support is carefully removed from the dissolution set-up with the casting resting along its top surface.

The wire is then attached to a holder, which later will serve as one of grips in the tensile testing apparatus. To do so, we used a micromanipulator (miBot™ from Imina technologies, Switzerland), which controls a fork connected to its arm, Fig. S-4(a). A critical moment in the whole procedure is the transfer of the wire lying on the filter onto the fork, Fig. S-4(b); this is carefully done by hand using precision tweezers under a binocular microscope, Figs. 4 (c-d). Then, using the micromanipulator, the wire is aligned with respect to the normal of the front side of the aluminium

grip, previously cleaned with ethanol in an ultrasonic bath, Fig. S-4(e). One extremity of the wire is placed on the flat part of the grip. Fig. S-4(f)), and its horizontal position is controlled by playing with the focus of the binocular microscope (error $\pm 5\ \mu m$). Once the wire is satisfactorily positioned, a drop of low viscosity cyanoacrylate glue (Loctite® 496™), which is particularly suited to bonding with metal substrates, is deposited, Fig. S-4(g). This gluing operation is repeated 2-3 times over an interval of 2-3 hours, Fig. S-4(h). For wires of diameter larger than $100\ \mu m$, in addition to the first drop of cyanoacrylate glue, a less viscous glue sensitive to ultraviolet light (Soliq) is used for the repeated gluing operations. From then on, the microcast wire is relatively easy to handle using the grip, and ready for characterization (by tensile testing, X-ray diffraction or scanning electron microscopy).
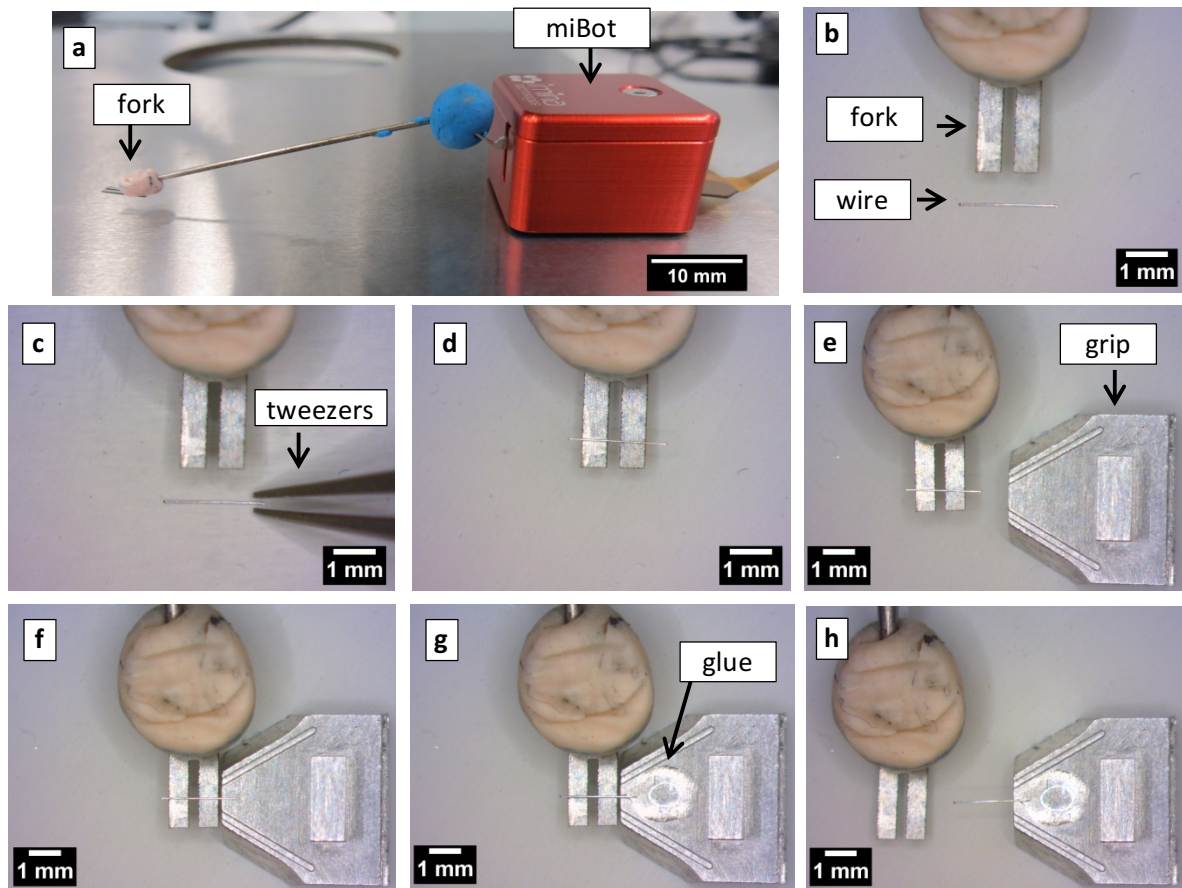

Figure S-4 - Photographs illustrating the different steps in the process of gluing a wire onto the small grip of the tensile machine. See text for more details.

2 Tensile tests and associated measurements

2.1 Detection and measurement of load drops

Figure S-5 shows a sample of the high-frequency (50 kHz) time-force signal that was measured with the LPM200 100 mN load cell in tension: at constant force (a), while testing a nylon fibre (b) and an aluminium microwire (c). As seen, for forces up to 20 mN these raw signals feature a significant level of noise with a standard deviation of 0.091 mN, independently of the instantaneous force value. Despite the relatively high noise, one sees that the signal measured at constant force, or when testing a nylon fibre, is relatively smooth, whereas sudden force drops can be clearly distinguished along the curve of the aluminium wire tested in tension. The drops are thus not an artefact of the testing device or procedure.

In order to obtain a workable signal, these data were filtered. The choice of the filter was based on the main requirement that the random noise must be reduced while the sharp steps marking sudden load drops must be retained. Based on these requirements a moving average filter was chosen as the one most faithfully recording both the flow stress and the displacement bursts. The filtered signal points (the output signal y) were thus calculated by averaging a number M of previous points in the raw signal (the input signal x) according to Eq. [S-1]:

$$y_i = \frac{1}{M} \sum_{j=0}^{M-1} x_{i-j} \qquad\qquad \text{Eq. S-1}$$

A four-pass moving average filter with M equal to 140 points was in this way applied to the raw data. Due to the unwieldy size of each saved file (tens of million data points) this multipass moving average filter was applied to data by intervals of 2 million data points (corresponding to 40 s of record) using a home-written LabVIEW program. Figure S-5(a'-c') shows the filtered signals corresponding to each of the raw signals plotted in Fig. S-5(a-c). One can observe that the filtered signals obtained at constant force and during the tensile test of a nylon fibre are smooth, as they should be. Conversely, the signal recorded during the tensile test of an aluminium microwire is highly intermittent. The jerky

flow stress observed during the test of the aluminium microwire is thus unlikely to be an artefact of the tensile machine setup and is rather a phenomenon related to the mechanical deformation of the aluminium wire itself. Note also that the standard deviation decreases from 0.091 mN for the raw force signal down to 0.007 mN for the filtered signal and from 0.185 mN down to 0.013 mN, respectively for the 10 g and 50 g LPM200 load cells.
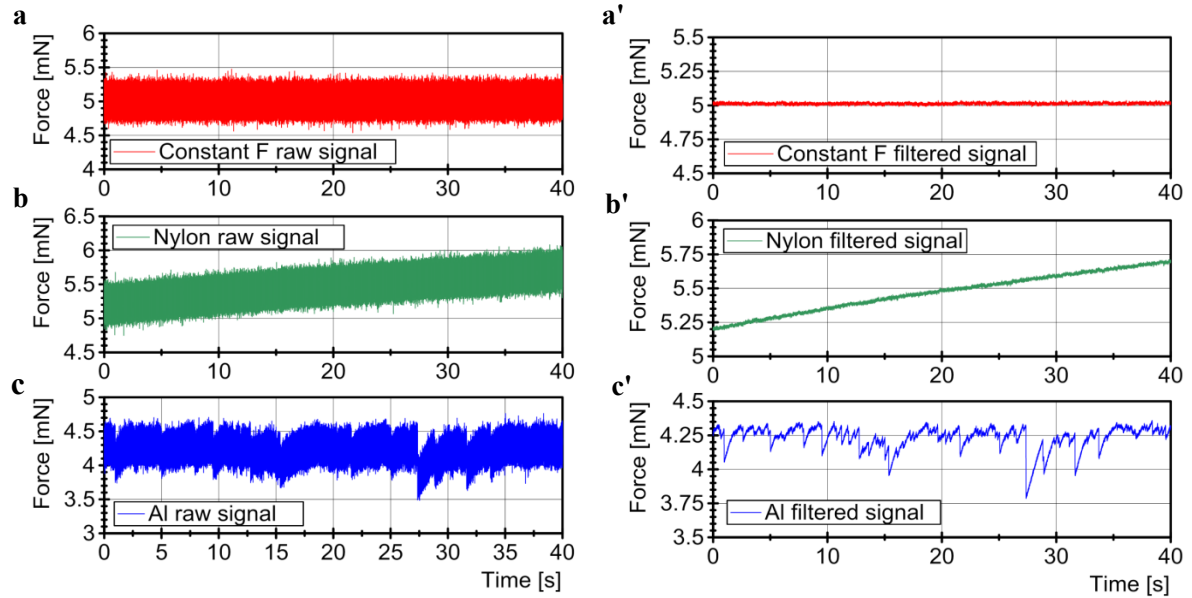

Figure S-5 - Raw and filtered force signal of the tensile machine. Comparison of the raw signal recorded during a test at a constant force (**a**), during a tensile test of a nylon fibre (**b**) and during a tensile test of an aluminium microwire (**c**). (**a'-c'**) Signal plotted in Fig. S-5(**a-c**) after filtering as described in the text.

From the filtered signal, load drop amplitudes were extracted based on measurements of the relative change in the difference between consecutive points. A combination of different parameters were used to certify that each detected load drop can safely be considered as such amidst noise in the signal; requirements for a drop to be counted as such were:

- an absolute drop size equal to or exceeding 0.075 mN (roughly ten times the standard deviation of the filtered signal);

- a drop size [mN] to drop duration [s] ratio above 6 mN/s on the filtered signal;

- a duration of intermediate fluctuations during the drop below 0.2 ms

If all three of these criteria were fulfilled for a force drop (as is the case for the drops indicated by the upwards pointing orange arrows in Fig. S-6(a), then the initial and final force values were recorded in

8

a separate file. Conversely, drops designated by the downwards-pointing black arrows in Fig. S-6(a) did not satisfy all the aforementioned criteria and were therefore not included in the file of recorded displacement bursts.

Figure S-6(b) shows a yet higher zoom onto the aluminium microwire stress-time curve in Fig. S-5(c'), this time focused on a single detected load drop. This plot combines raw (grey) and filtered (red) signals. The force-filtered signal is shifted in time by roughly 0.004 s: this is an (inconsequential) artefact caused by the fact that the filter uses a left-sided moving average (see Eq. S-1). A more important influence of the moving average filter is that the force drop rate is decreased; however, in the present context this is not important since we only examine the amplitude of each load drop. The black squares in Fig. S-6((b) show the start and the end of the load drop on the figure; as seen, taking into account the horizontal shift caused by the moving filter used, the location of these two points is consistent with the raw data.
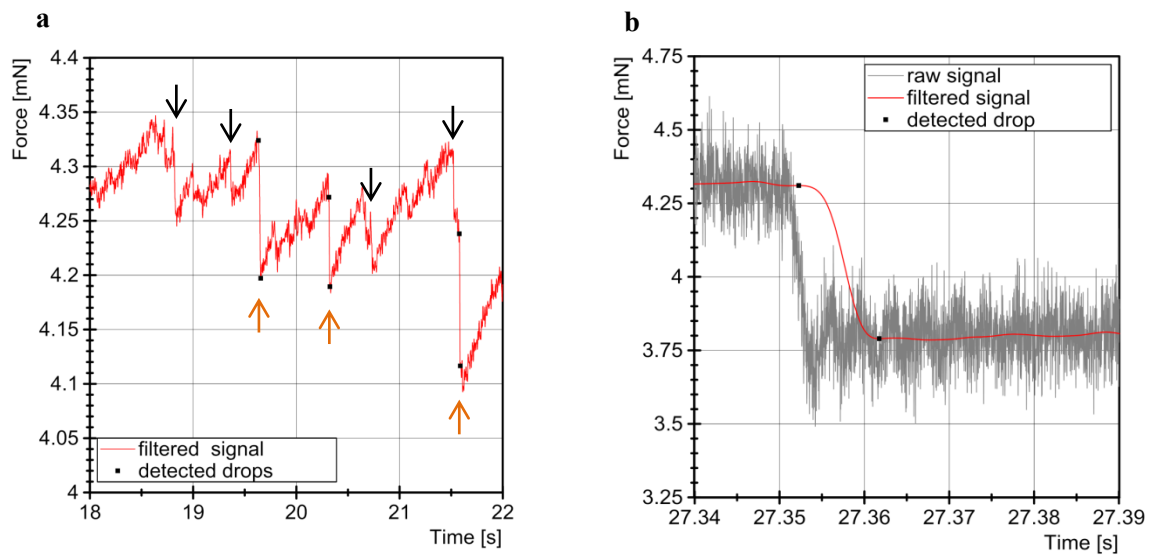
Figure S-6 - Detection of load drops. (**a**) Zoom between 18 and 22 s on the filtered signal of Fig. S-5(**c'**). The downwards black arrows show load drops that do not qualify as displacement bursts because they do not satisfy all criteria. The upwards orange arrows indicate the validated displacement bursts, for which the black squares designate the measured start and end of the drops. (**b**) Zoom on the large load drop occurring just after 27 s in the bottom curve of Fig. S-5(**c'**). The moving average filter causes a shift in time of the signal.

Load drop data collected in this manner were then used to investigate the statistical distribution of larger displacement bursts in each deforming sample. To do so, the size of each displacement burst *s*

resolved in the primary slip system was calculated from the corresponding detected load drops ΔF using the following relation:

$$s = Nb = \frac{\Delta F}{S \cos \lambda} \qquad \text{Eq. S-2}$$

where N, b, S and λ are respectively the number of dislocations involved in the burst, the Burgers vector of aluminium, the stiffness of the entire tensile system including the sample and the angle between the loading axis and the primary slip direction. For this calculation, the displacement of the motor during the load drop was neglected since the displacement rate associated with the load drops is roughly 1000 higher than the displacement rate of the motor (running at 300 nm/s).

To explore the distribution of the displacement burst sizes, we used (as is commonly done) the cumulative distribution function $P(x<X)$, which is the probability that x have a value smaller or equal to X [S-2]. Specifically, we plot here the complementary cumulative distribution function $P(x>X) = 1-P(x<X)$, also called rank/frequency plot; this is simply obtained by ranking all the events by descending size along a horizontal axis of their intensity, numbering them in that order, and plotting on the vertical axis that number divided by the total number of events. The resulting value corresponds to the probability that x be greater than X, i.e. the complementary cumulative distribution function $P(x>X)$. These data were then plotted using either logarithmic or semi logarithmic scales. Reported values of β were calculated by fitting an exponential distribution to that portion of the entire dataset for which $0.1 \leq P(x>X) \leq 1$.

2.2 Measuring the system-*cum*-sample stiffness and testing data for the cutoff predicted by dislocation avalanche theory

The load train stiffness S [mN/µm], which relates the drop in force with the (absolute) load train displacement, is used in Eq. S-2 to calculate the displacement burst size s, and is also used in analysis of the mechanical data to calculate the contribution of the plastic shear displacement to the total displacement so as to only plot the former. Values of S for each experiment were calculated from

measured values of the linear part (the initial straight portion) of the force-displacement curve knowing the (relatively isotropic) Young's modulus of aluminium. Results are given in Table S-1.

Note that S differs from M [MPa], the (strain-based) stiffness that enters the equation of Zaiser and Nikitas mentioned in the main part of the text. M and S are mathematically linked according to $M = \frac{S\,L_i m^2}{A_0}$ with L_i the initial gauge length, m the Schmid factor and A_0 the cross-sectional area of the sample. Since in the calculations of Zaiser and Nikitas and those of Csikor et al. [24,31] the samples were roughly as tall as they were wide, we have taken L_i equal to the sample diameter. Results for all samples of this work are in Table S-1; as seen predicted cut-off values are just a bit smaller than measured values, but near the right order of magnitude of one micrometer.

Ø [µm]	[h k l]	L_0 [µm]	$\gamma_{failure}$ [-]	S [mN/µm]	M (L_i=Ø) [MPa]	H [MPa]	Δl_{max} [µm]	Δx_{max} [µm]
6	[1 2 1]	580	0.245	0.71	25.13	0.6	0.59	0.68
7	[0 7 3]	510	0.031	0.66	29.03	-	0.63	0.97
6.8	[4 6 3]	765	0.514	0.65	21.62	4.6	0.60	0.73
6.7	[1 5 3]	4810	0.097	0.61	27.89	-	0.65	0.91
7	[3 -2 7]	1210	0.063	0.44	18.15	-	0.97	1.20
6.7	[-3 -7 1]	620	0.055	0.60	28.20	-	0.66	0.89
13.1	[3 3 4]	1520	0.480	0.75	8.29	166.5	0.07	0.08
13	[-4 3 3]	1300	0.272	0.58	6.47	96	0.12	0.14
14.8	[1 7 1]	1260	0.274	0.70	12.18	4.4	1.01	1.27
14.3	[-1 1 1]	700	0.526	0.81	5.33	161.3	0.06	0.07
13.6	[1 6 -1]	730	0.327	0.84	15.94	4.9	0.80	1.00
14.1	[3 5 1]	820	0.367	0.91	42.13	1.8	0.61	0.85
15.2	[1 1 2]	1480	0.265	0.81	11.29	78	0.17	0.20
19.4	[3 0 1]	1456	0.420	0.85	13.45	3.8	1.06	1.57
19.9	[2 7 1]	840	0.443	0.98	14.62	3.9	0.97	1.26
19.8	[-1 1 4]	1120	0.438	0.90	11.95	3	1.13	1.35
18.8	[0 1 1]	1428	0.905	0.95	10.68	1.5	1.25	2.49
19.4	[1 1 0]	2073	0.709	0.62	6.77	5.7	1.22	2.43
18	[1 1 0]	1951	0.928	0.72	8.53	4.8	1.14	2.28
103	[3 4 -1]	1630	1.35	2.46	6.75	5.7	1.41	2.03

Table S- 1: Overview of general parameters of tested microwires showing sample diameter Ø, sample axis orientation, initial gauge length (L_0), shear strain to failure ($\gamma_{failure}$), stiffness (S), M as calculated from S assuming L_i=Ø, and the measured work hardening rates H. Note that for diameters < 7 µm not all work hardening rates could be measured. Δl_{max} is the predicted length increment cut-off based on the calculations in Zaiser and Nikitas and those of Csikor et al. [24,31]. Δx_{max} corresponds to a projection in the slip plane of the calculated length increments.

2.3 Evolution of dτ/τ during a load drop

A single-crystalline wire with its axis oriented along the *z* direction and having a cross-sectional area *A* is subjected to a force *F* along its axis, Fig. S-7(a). In single-glide (Stage I) deformation, the wire elongates by glide along a plane making an angle ϕ between its normal *n* and *z*, and along a direction forming an angle λ with *z* as shown in Fig. S-7(a). While gliding, the total sample length ΔL increases by an amount linked to the slip distance *l* by:

$$\Delta L = l \cdot \cos \lambda \qquad\qquad \text{Eq. S-3}$$

The projection onto the slip plane of the wire's circular cross-section, of area *A*, in the *x-y* plane has an area:

$$A' = \frac{A}{\cos \phi} \qquad\qquad \text{Eq. S-4}$$

Due to slip, the remaining contact area A'' between the two parts of the wire on either side of the slip plane can be calculated relatively simply by projecting both the upper and lower parts of the slip plane back onto the *x-y* plane as shown in Fig. S-7(b) and recalling that area ratios are unchanged after projection. The upper and lower surfaces have slipped one with respect to the other by a distance l_x along b_x; this results in a decrease of *A* by:

$$A'' = 2 \cdot R \cdot l_x = 2 \cdot R \cdot l \cdot \sin \lambda \qquad\qquad \text{Eq. S-5}$$

A slip step *dl* therefore causes a relative decrease in the contact area between the upper and lower surfaces of:

$$\frac{dA'}{A'} = \frac{dA}{A} = \frac{-d(2 \cdot R \cdot l_x)}{\pi \cdot R^2} = \frac{-2 \cdot \sin \lambda \cdot dl}{\pi \cdot R} \qquad\qquad \text{Eq. S-6}$$

The slip step is thus associated with a relative decrease in force caused by (elastic) unloading of the sample plus apparatus load train equal to:

$$\frac{dF_x}{F_x} = \frac{-dL}{C \cdot F_x} = \frac{-\cos \lambda \cdot dl}{C \cdot F_x} \qquad\qquad \text{Eq. S-7}$$

where C is the compliance of the entire system, including both the sample and the load train. At the simplest level of analysis (neglecting for example any rotation of the slip plane, which is legitimate given the high wire aspect ratio, or effects of stress concentration), the average shear stress τ on the remaining cross-sectional area of the sample in the glide plain hence evolves as:

$$\frac{d\tau}{\tau} = \frac{dF}{F} - \frac{dA}{A} = \left(\frac{-\cos\lambda}{C \cdot F} + \frac{2 \cdot \sin\lambda}{\pi \cdot R} \right) dl \qquad \text{Eq. S-8}$$

The evolution of the average shear stress τ during load drops calculated from Eq. S-8 is represented in Fig. S-8. This graph shows that, during a load drop, there is a relaxation of the average shear stress driving dislocation motion in the glide plane that is generally of 20% or less, reaching at most 35% in a few of the largest amplitude strain jumps for 7 µm diameter wires. This relatively small decrease in applied resolved stress during a large strain jump occuring on a single glide plane is to be contrasted with what happens with a stiff set-up (where the load will decrease faster given the lower value of C) or a very compliant set-up (where τ will actually increase because of the reduction in glide plane area).
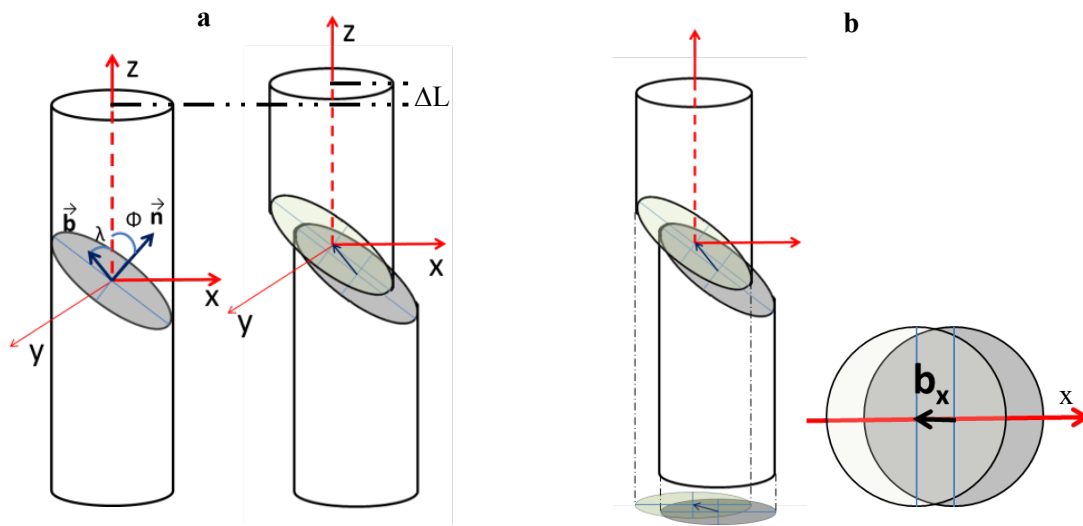

Figure S-7 - Geometry of concentrated single slip. Schematic illustration showing a wire gliding along one plane (**a**). The projection on the x-y axis of the glide plane (**b**).
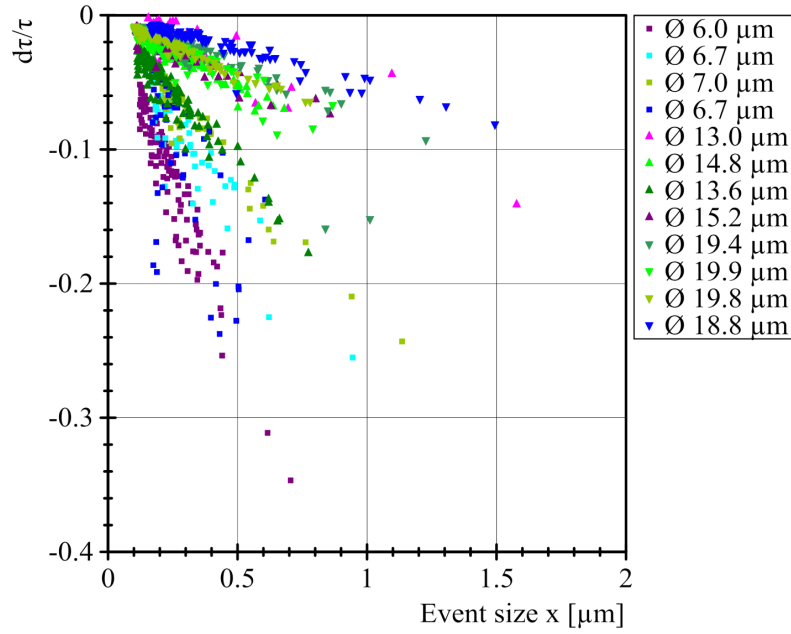
Figure S-8 - Shear stress variation during a load drop. The variation of the resolved shear stress during the load drops as calculated from Eq. S-8. For clarity, not all sample data are plotted.

2.4 Microwire tensile test data

Plots of all tensile data from the wires and the wire crystallographic orientations are given in Fig. S-9, in four plots sorted according to the wire diameter. In the plot with the largest (≈ 100µm) diameter wires, we have added two curves from the literature for macroscopic <011> or <145> ("bulk") aluminium single crystals [29].
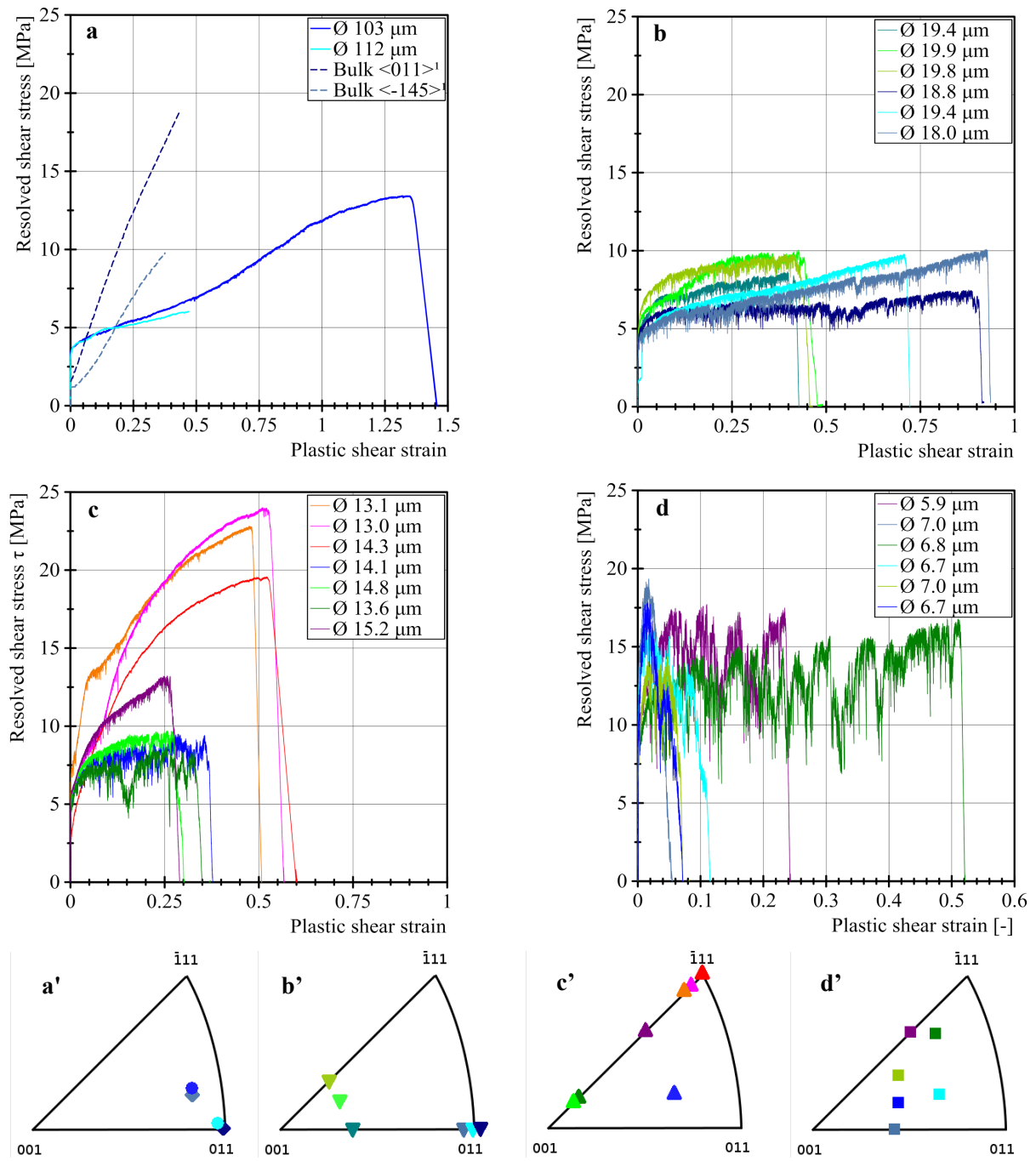
Figure S-9 - Tensile curves of microcast Al wires. Resolved shear stress versus the resolved plastic shear strain of the 100 μm (**a**), 18-20 μm (**b**), 13-15 μm (**c**) and the 7 μm (**d**) diameter aluminium wires. The axis orientation of each of these wires was measured by Laue diffraction and is given in the standard stereographic triangle by upwards pointing triangles and downwards pointing triangles for 100 μm cast microwires (circles) and bulk aluminium (lozenges) (**a'**), 18-20 μm microwires (downward pointing triangles) (**b'**), 13-15 μm (**c'**) and the 7 μm (**d'**) diameter wires respectively.

2.5   Displacement burst statistics across all event sizes

We repeated the displacement burst detection and size statistical analysis, using the same detection algorithm, but after adapting it by placing the lower limit of detectable load drops at the noise level

of the filtered signal (=0.007 mN), and after altering displacement burst selection criteria to include all events such that:

- The drop size [mN] to drop duration [s] ratio is above 1 mN on the filtered signal.

- The duration of intermediate fluctuations during the drop is below 0.2 ms (to make the distinction between having one big drop and two sequential drops).

If these (far more liberal) criteria were fulfilled for a force drop then the initial and the final force values were recorded. In this manner we detect many more 'drops' than are in reality present; however, one can assume, as is often done, that apparent drops emanating from signal noise have a Gaussian distribution and will show up as such on plots of size distribution if compared to real drops, presumably distributed according to a powerlaw with an exponential cut-off.

Resulting data are reported in Fig. S-10. As seen, this reproduces what is generally found in the literature:

- a first part is Gaussian in shape and likely represents noise in the signal

- then one finds a portion of the curve that appears to be relatively straight on these log-log plots.

Providing evidence for scaling in the lower-amplitude portion of the measured burst size distributions. The extent of this portion, which spans about one order of magnitude in event size, is lower than for data recorded with micropillars compressed under a nanoindenter. The slope of the linear portion of the curves, which is generally between 1 and 2 for the various samples, is in line with earlier data recorded with nano- or micropillars (see e.g., Fig. 7 of Ref. [S-11]).
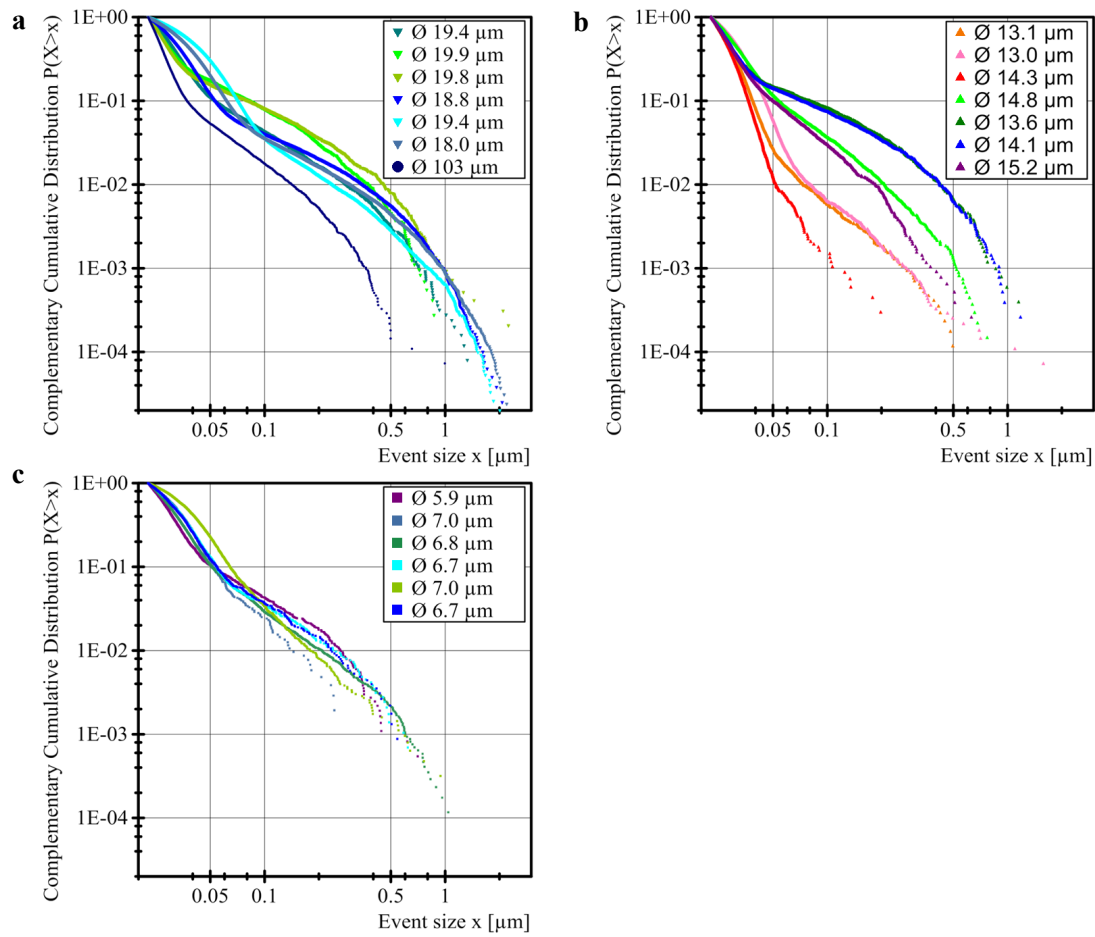
Figure S-10 - Complementary cumulative distribution function of all detected dislocation avalanche sizes, with event size expressed in terms of slip distance along the glide direction and plotted in log-log coordinates, for the same samples as in Fig. 5: distribution of data in (**a**) distribution of the 18-20 µm, (**b**) 13-15 µm and (**c**) 6-7 µm diameter wires plotted in semi-logarithmic coordinates.

3   Transmission Electron Microscopy

(conducted with significant help from Dr. Marco Cantoni and Dr. Emadeddin Oversi at EPFL's

Interdisciplinary Center for Electron Microscopy)

Dislocation microstructures in samples cut out from wires and thinned using focused ion beam

milling were observed in transmission electron microscopy (TEM).

Two samples were cut normal to the axis of as-cast 14 µm wires and one sample was extracted from

an as-cast 7 µm wire. The lamellae were prepared by FIB milling in a Zeiss Nvison 40 dual-beam

Focused Ion Beam (FIB)/Scanning Electron Microscope (SEM) using a Ga+ source. Once the spot

where the TEM lamella was to be cut along the wire was chosen, Fig. S-11(a), a layer of carbon

roughly 1 μm thick was deposited at the surface in order to protect the wire from FIB damage. Then the free extremity of the wire was cut and a trench was milled at its other extremity, Fig. S-11(b). The last part of the trench was milled once a nanomanipulator was attached to the specimen slice, Fig. S-11(c). The latter was subsequently moved and attached by carbon deposition onto a copper grid, Fig. S-11(d). The last step of the process consisted in thinning the lamella down to around 300 nm so as to make it electron-transparent, Fig. S-11(e); this was performed using 30 keV Ga$^+$ ions and a final (low) milling current of 80 pA. In order to clean the surface from redeposition of sputtered atoms, a final cleaning step was performed by ionic bombardment at 5 keV. Note that two thicker bands on both side of the lamella were left to strengthen the sample and avoid bending, Fig. S-11(f). The lamellae attached to their copper grid were observed on a 120 keV Philips/FEI CM12 transmission electron microscope both in dark and bright field imaging. Figure C shows a bright field TEM image of the entire lamellae for an as-cast sample.
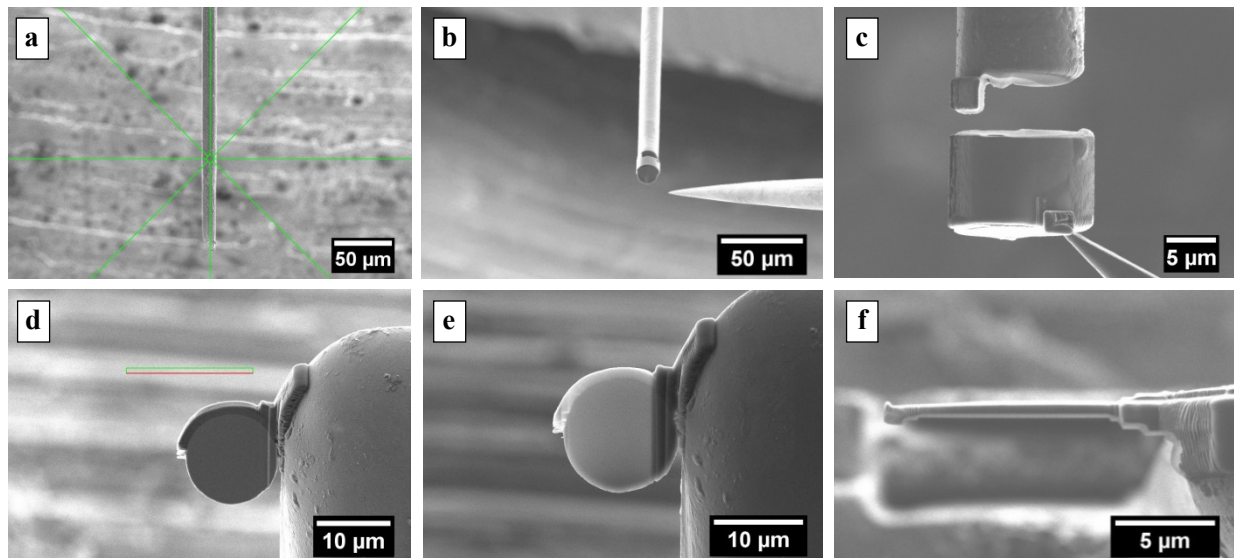

Figure S-11 - FIB milling of a TEM lamella. SEM images showing steps used for the fabrication of a transverse TEM lamella from a wire in the as-cast condition. Wire showing the spot where the TEM lamella was cut (**a**). A protective layer of carbon roughly 1 μm thick was deposited at the surface, the free extremity of the wire was cut, and a trench was milled at the other extremity (**b**). The last part of the trench was milled once the nanomanipulator was attached to the specimen slice (**c**). The latter was subsequently moved and attached by carbon deposition onto a copper grid (**d**). The lamella was thinned down to around 300 nm, making it electron transparent (**e**). Two thicker bands on either side of the lamella were left to prevent bending in subsequent sample manipulation or transport (**f**).

The same procedure, namely carbon coating, milling, transfer to the copper grid and thinning, was used to prepare a thinned sample from a deformed wire 15.2 μm in diameter with a [112] axis orientation. The TEM lamella was cut parallel to the observed glide plane and milled somewhat

differently to the as-cast wire samples (the cross-section being elliptical); observation was conducted using a 200 keV FEI TecNaI Osiris (S)TEM microscope. Another sample was cut at 45° to the axis of a 6.8 μm deformed aluminium wire of axis orientation [463]; however, structures were highly inhomogeneous across the lamella, indicating that it was damaged (likely by bending) during sample preparation; those data were hence discarded.
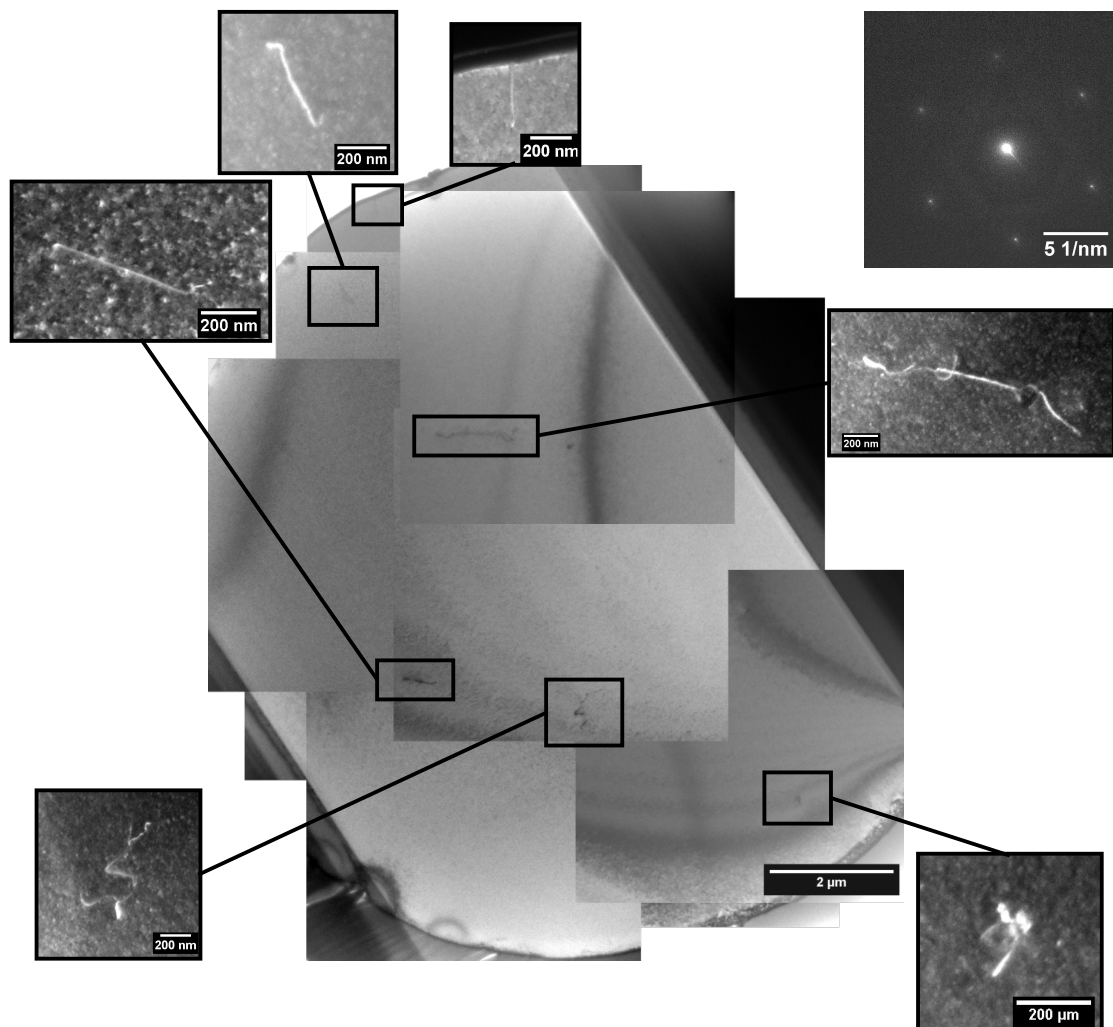

Figure S-12 - TEM image of an as-cast Al wire. The central image is a bright field TEM image of the foil of an as-cast sample taken along a <111> zone axis, giving the diffraction pattern at the top right. Around the central image are dark field TEM images taken at g = {011} and representing the observed dislocations in the foil.
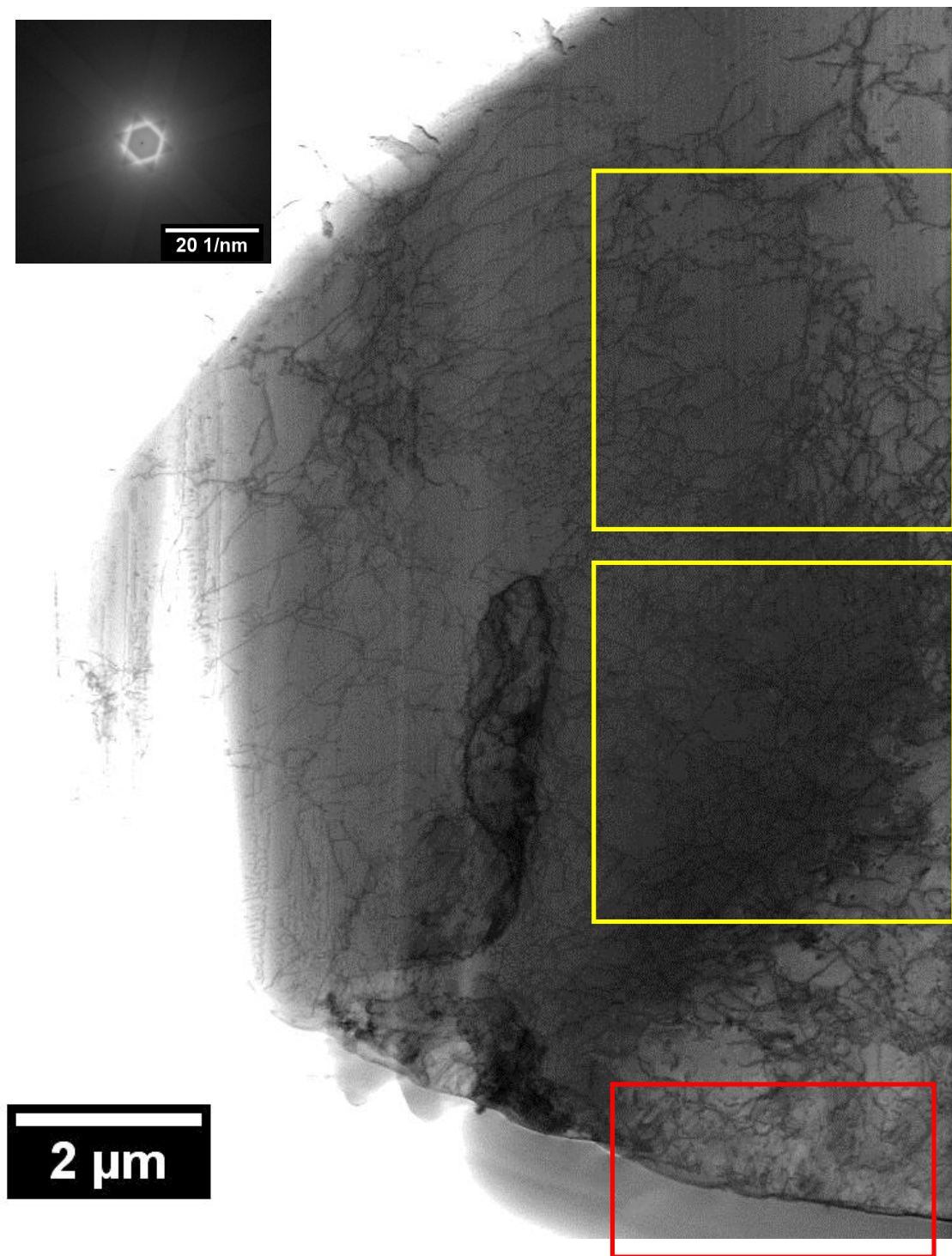
Figure S-13 (overleaf) - TEM image of a deformed Al wire. Bright field STEM image of the 15.2 μm diameter aluminium wire deformed in tension, taken along zone axis <111> as shown in the diffraction image in the top left corner. The foil is parallel to a {111} plane that was activated during plastic deformation. The vertical linear side of the lamella on the left side of the image indicates that during the FIB milling the surface glide step was reached. The left part of the foil was not covered by a carbon protective layer; as a consequence, the left side of the lamella is more likely to have been damaged during milling and was not analysed. On the right part of the foil, a large number of dislocations can be observed. The invisibility conditions at the <111> zone axis were unfortunately such that we could not identify the Burgers vector of these dislocations. Their density was measured in the two areas delineated by yellow squares. The area outlined by the red rectangle at the bottom was used for EDX characterization of the surface; results are in Fig. S-14.
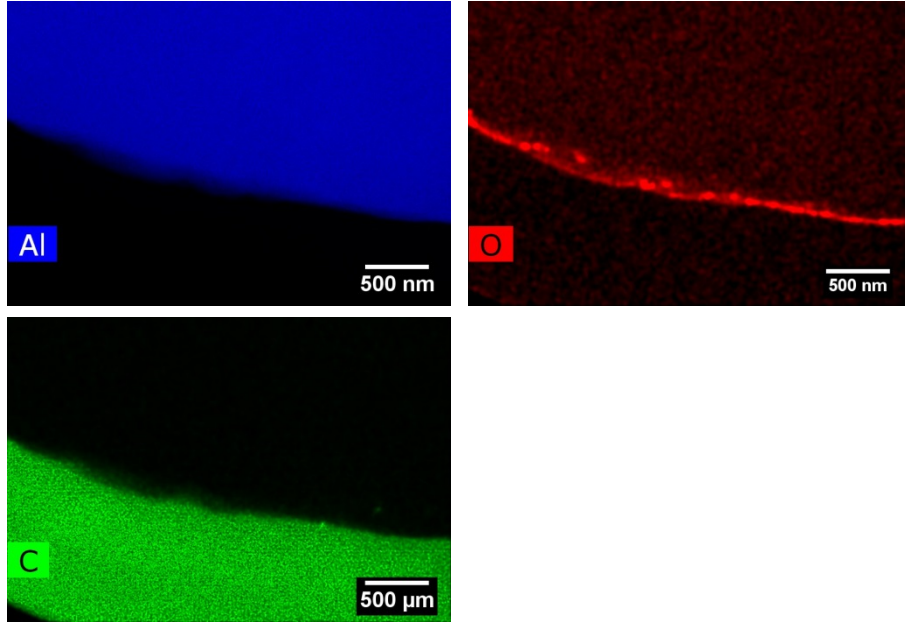
Figure S-14 - EDX STEM mapping of an aluminium wire surface. EDX STEM elements mapping of aluminium Al, oxygen O and carbon C performed over the zone delineated with a red rectangle in Fig. S-8.

A general view of one of the thinned as-cast 14 μm diameter wire cross-sections is given in Fig. S-12 (the other as-cast specimen was similar). The deformed 15.2 μm diameter deformed specimen cross-section is shown in Fig. S-13. Using the TEM images, the density of dislocations was estimated for the as-cast and deformed wires. In as-cast samples, given the low density of dislocations, this was done by manually tracing and measuring the total visible dislocation line length L_d, corrected for the inclination of the TEM stage when the photograph was recorded, over a defined area A of thickness t_L:

$$\rho = \frac{L_d}{A t_L}$$

Eq. S-9

To trace and measure the length lines, freeware *ImageJ* was used. The lamella thickness t_l was measured from a SEM image of a transversal view of the lamella as shown in Fig. S-11(f). Most of the observed dislocations are straight and are randomly dispersed within the foils. The two as-cast TEM foils contain only a few dislocations corresponding on average to a dislocation density $\rho = 1.2 \times 10^{11}$ m^{-2} (1.4×10^{11} m^{-2} and 9.4×10^{10} m^{-2} respectively for each of the two 14 μm diameter slices of as-cast metal). The TEM lamella cut in the 7 μm diameter wire contain a slightly higher dislocation

density, namely $\rho = 1.4 \times 10^{12}$ m^{-2}. These measurements have different sources of error; one is error in the foil thickness. The thickness of the foil was measured on a SEM image of the top view of the lamella; however, TEM lamellas produced by focused ion milling usually have a taper resulting in a variation in thickness through the lamella. We estimate this error to be of $\pm$ 20 nm on the measured lamella thickness. Secondly, there is an error on the measurement of the length of the dislocations on the TEM images, both in measurement and in the fact that these segments possibly underwent rotation. Finally it is possible that segments of dislocations perpendicular to the foil were missed because these were confused with FIB damage consisting in dislocation loops.

That the microcast wires be so free of thermal dislocations typical of cast and cooled multiphase microstructures of this scale is *a priori* surprising, given that NaCl and Al have widely different thermal expansion coefficients (4.05×10^{-5} K^{-1} and 2.35×10^{-5} K^{-1} respectively), and that microporous aluminium produced by replication (also involving infiltration of packed salt particle preforms) betrays the presence of extensive thermal dislocation emission after cooldown in a processing cycle similar to that used to infiltrate salt moulds in the present work [S-3]). To explain this difference the shape of the present convex cylindrical aluminium microcast crystals can be invoked: these are convex ellipsoids and, unlike fine-scale microcellular metal structures, experience in principle no thermal strain gradients as they cool.

In the deformed wire specimen far higher dislocation densities were observed, Fig. S-13. The line-intercept method was therefore used to assess ρ, knowing the foil thickness (460 nm) by prior measurement during the sample preparation procedure. Results for the two square regions indicated in Fig. S-13 are $\rho = 1.8 \times 10^{13}$ m^{-2} and $\rho = 1.7 \times 10^{13}$ m^{-2} respectively, with an estimated uncertainty on the order of 5×10^{12} m^{-2}.

EDX STEM elements mapping of aluminium Al, oxygen O, carbon C and gallium Ga along the deformed wire surface are presented in Fig. S-14; these show the metal to be covered by the carbon protective layer and between the carbon and the metal, data show the presence of a layer roughly 5 nm wide containing oxygen along the surface of the wire, consistent with observations made with

microcellular aluminium produced by the (closely related) replication process produced using the same chromate corrosion inhibitor as was used here [S-4].

In conclusion, in the 14 μm diameter microcast wires the initial dislocation density takes a low value, $\rho \approx 1.2 \times 10^{11}$ m^{-2}, and increases by two orders of magnitude after deformation. Note that this feature of wire deformation was also captured by large scale dynamic discrete dislocation modeling, as illustrated in Fig. S-15.

4   3-D DD simulations and dislocation structure analysis

4.1   Analytical single-arm source models

The equation used for the single-arm source model in Fig. 2d of the main text is as follows:

$$\tau = 0.12\mu\ln(L/b)/(L/b) + \mu b(\Sigma_u\, a_u\rho_u)^{1/2} \approx 0.12\mu\ln(L/b)/(L/b) + 0.44\mu b\rho_f^{1/2} \qquad \text{Eq. S-10}$$

The first term on the right-hand side is the single arm source component and the second term is the classical forest hardening component. It has been assumed that these two contributions are linearly additive. The pre-factor 0.12 used for the single-arm source component is obtained from dislocation dynamics calculations [S-5, S-6]; however, in simulations it can vary from 0.068 to 0.148, depending on the angle between the Burgers vector and line direction of the single-arm source. In the equation, b is the Burgers vector of the gliding dislocation, ρ_u is the dislocation density on slip-system 'u' and a_u is the forest-interaction coefficient between slip system 'u' and the gliding slip system. The forest-interaction coefficients a_u have been taken from previous dislocation dynamics simulations [S-7, S-8] as 0.045, 0.13, 0.13 and 0.854 for the Hirth lock, Glide lock, Lomer lock and Colinear lock forming forest slip systems, respectively. ρ_f is the total forest dislocation density and is equal to $0.75\rho_t$ where ρ_t is the total dislocation density. Figure 2d of the main text takes $\rho_t \sim 6 \times 10^{11}$/m^2 for Model 1 and $\rho_t \sim 2 \times 10^{12}$/m^2 for Model 2 (approximately the dislocation density measured in the wires by transmission electron microscopy, see above). These are also the initial total dislocation densities in the present large-scale 3D dislocation dynamics simulations in Fig. 2d (respectively Simulation 1 and

. The detailed distribution of initial dislocation density, slip system by slip system, ρ_u, is given in Table S- 2. Note that, at this initial dislocation density, the hardening predicted in 100 μm microwires, where the single-arm source strengthening contribution is negligible, is close to experimental values. The effective length of the single-arm source at initial yield, 'L', has been taken to be D/3 in Fig.2d, where D is the diameter of the wires; we note, however, that the single-arm source model proposed by Parthasarathy et.al. [S-9], for a sample aspect ratio of 100 and an initial dislocation density of 6×10^{11}/m^2, would suggest an effective single-arm source length of D/2 at initial yield.

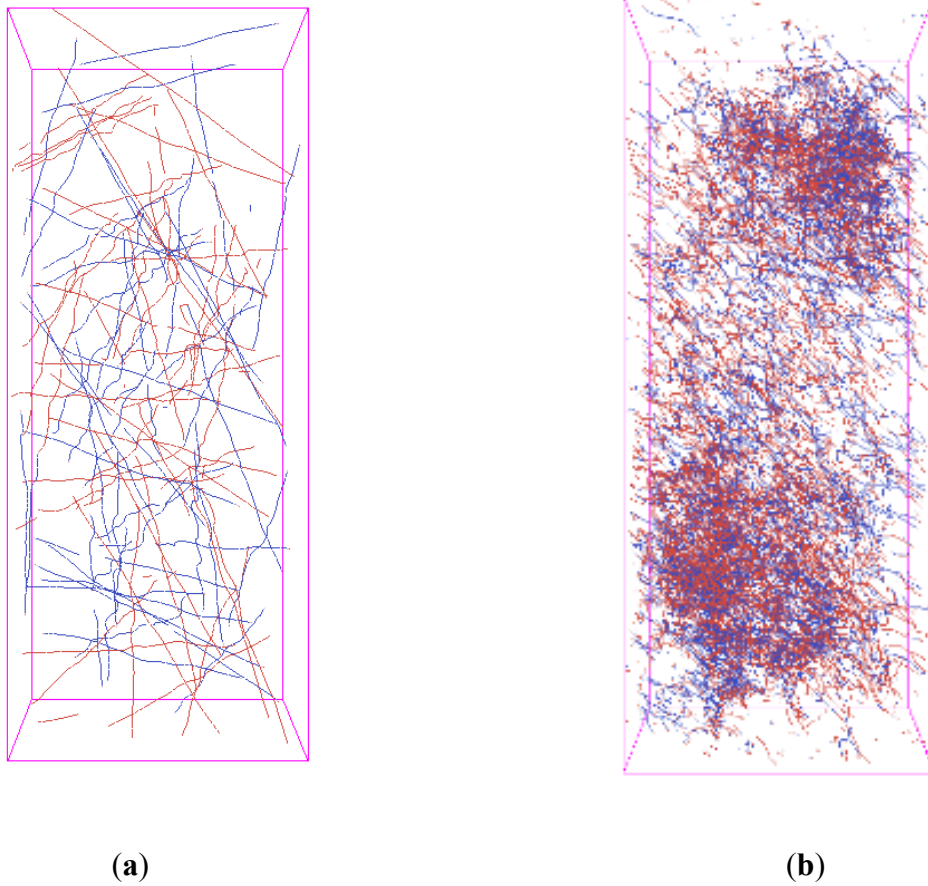(**a**)   (**b**)

Figure S-15 - Simulated dislocation structures. Dislocation microstructure from 3D dislocation dynamics on two active slip systems (denoted by blue and red colours), (11-1)[011] and (1-11)[011], (**a**) initial, (**b**) after deformation to 0.003 strain, for the [001] orientation, in a 20 × 20 × 50 μm FCC micropillar, accounting for physically based cross-slip mechanisms.

Slip system	Dislocation density (X E^{10}/m²), 20μm	Dislocation density (X E^{10}/m²), 6μm
(111)[1-10]	4.92	4.52
(111)[10-1]	4.46	4.36
(111)[01-1]	4.56	5.92
(-111)[110]	4.47	3.62
(-111)[101]	4.29	4.46
(-111)[01-1]	5.49	3.47
(1-11)[110]	4.17	4.43
(1-11)[10-1]	6.06	5.49
(1-11)[011]	4.55	5.84
(11-1)[1-10]	5.07	5.77
(11-1)[101]	4.45	3.80
(11-1)[011]	4.54	5.77
Non-FCC	0.6	0.4

Table S-2: The dislocation density on various slip systems after 100 iterations in the 20 and 6 μm FCC crystal 3D dislocation dynamics micropillar simulations described in the manuscript.

Predictions of this single arm source model for the plasticity size effect at 6 and 20 μm wire diameters are in good agreement with experiment; however, one should bear in mind that there are several uncertainties in the model, such as (i) the effective L value (assumed as D/3) [S-9], (ii) the pre-factor for single-arm source strengthening, assumed here as 0.12 [S-5,S-6] but given different values elsewhere [S-10], (iii) the assumed linear additivity of single-arm source strengthening and classical forest hardening, as well as (iv) uncertainties in the forest-interaction coefficients a_u [S-7,S-8].

4.2   Load –controlled deformation in DD simulations

In DD simulations, the crystals were strained in tension under displacement control along three multi-slip directions, namely <111>, <001> and <110>, at a constant strain rate of 10/s. In this mode of loading, if the movement of dislocations at a timestep 't' led to a plastic strain rate higher than 10/s, the applied strain rate in the simulations, then the stress was decremented, such that the total strain rate (plastic strain rate + elastic strain rate) was exactly equal to 10/s at that timestep.

Some 6 μm simulations were performed after adapting this deformation-controlled model to mimic load-control, as this is more representative of experimental conditions in this work. In load-control

mode, the stress was not allowed to drop: it was kept a constant whenever the plastic strain rate exceeded the applied strain rate of 10/s. Then, the stress was incremented only after the total strain at time t (elastic strain plus plastic strain) became less than $10t$, where t is the time of deformation, signaling that the load train had caught up with the sample deformation, or in other words that the sudden displacement burst had ended. Therefore, for a displacement burst to end in the simulations, the plastic strain rate was not required to go to zero, but only to an average value less than the applied strain rate, meaning to a value such that the condition (elastic strain + plastic strain) < $10t$, where 't' is the time of deformation and 10 is the overall applied strain rate, be satisfied.

The consequence of this change in loading mode during the simulations is a significant increase in the magnitude of displacement bursts recorded; see Fig. 3 in the main text. Also, during a displacement burst in Fig.3c for 6 μm pillars (load-control), the plastic strain rate was at least equal to the applied strain rate 10/s for some portion of the burst. If a single single-arm source operates at an average velocity v m/s in a pillar of length L and square cross-section side D, then it will generate a tensile strain rate at most $\approx 0.4(vb/DL)$ s^{-1} where b is the Burgers vector. In the present DD simulations, the velocity of the dislocations is linearly proportional to the stress on the dislocations and is 1 m/s at a stress of 1 MPa. The shear stress applied on the source is at most ~ 15 MPa (see Fig.3c), such that over a pillar 50 μm long and 6 μm in diameter (as assumed in the simulations) a moving single arm source will produce strain rates of at most ~ 5 /s. This is why in the simulations, more than one independent single-arm source needs to operate to achieve a plastic strain rate of 10/s, and _a fortiori_ for a plastic displacement burst to initiate in the simulations. This is seen in both Movies 3 and 4 described below. In experiments, where the applied strain rate is much smaller, ~ 0.002/s, even though the specimen length is far greater (1mm), a single arm source is sufficient to generate a visible sudden displacement burst.

4.3 Films

Films can be seen in SI files from two simulations performed with an initial total dislocation density of ~ 6×10^{11}/m^2. Each movie is accompanied by some images showing the stress-strain curve indicating

the range covered by the film and detailing a few features in the movies. 3D dislocation dynamics data were collected every 100 timesteps, and 1/100 of these data (1 out of every 100 data files) over the strain burst was used to generate the movies; hence there are likely many more turns of the sources in the simulation than can be seen in the movies. The total number of turns N by all sources required to generate the "filmed" strain bursts is $N \approx 500$ for the [001] movie, and $N \approx 1,500$ for the [110] movie.

4.3.1 [001] movie, part-cell

Dislocation microstructure evolution in a 6 × 6 × 50 µm pillar, stressed along the [001] orientation, at shear strains of 0.014 - 0.017. Dislocations on all slip systems are shown. Note the operation of (1-11)[011] sources (whitish orange) and their frequent cross-slip onto the (11-1)[011] slip system [red]. One of the (1-11)[011] sources ceases to operate by partially cross-slipping onto the (11-1)[011] slip system and by interaction with dislocations from other slip systems.
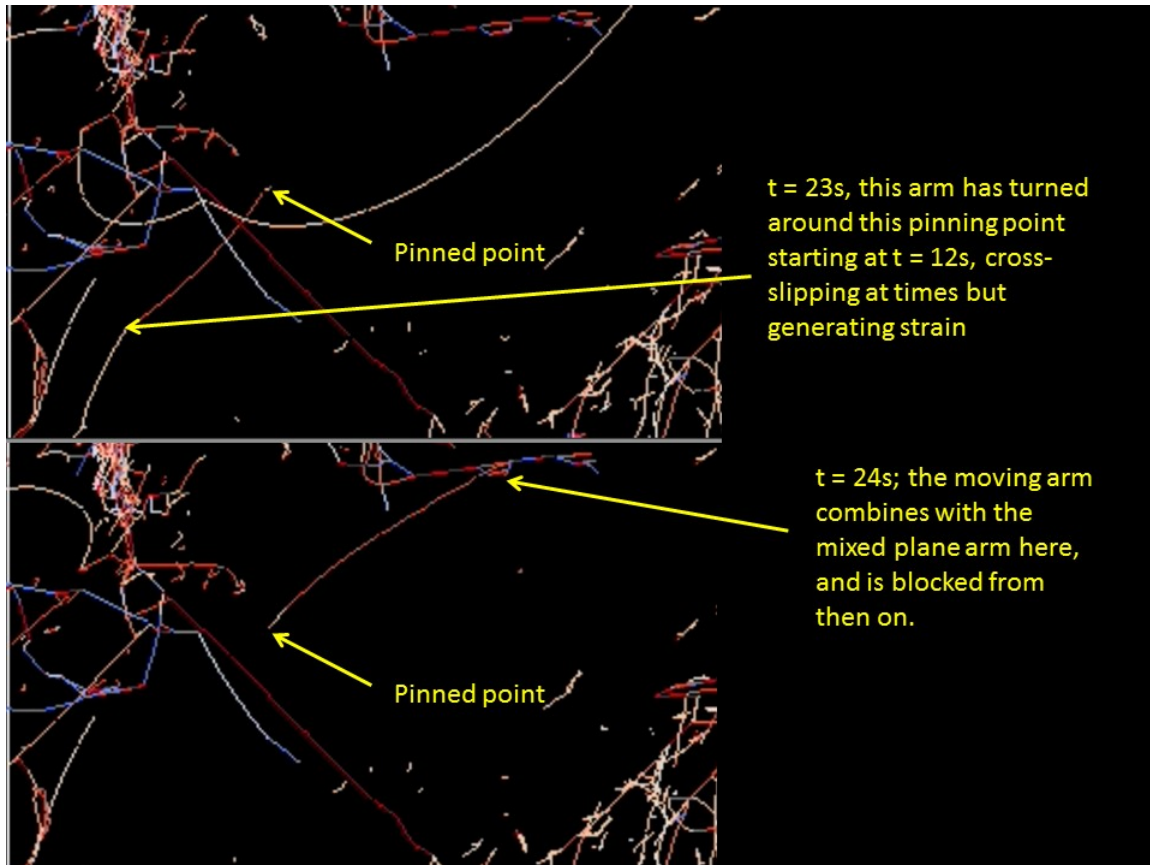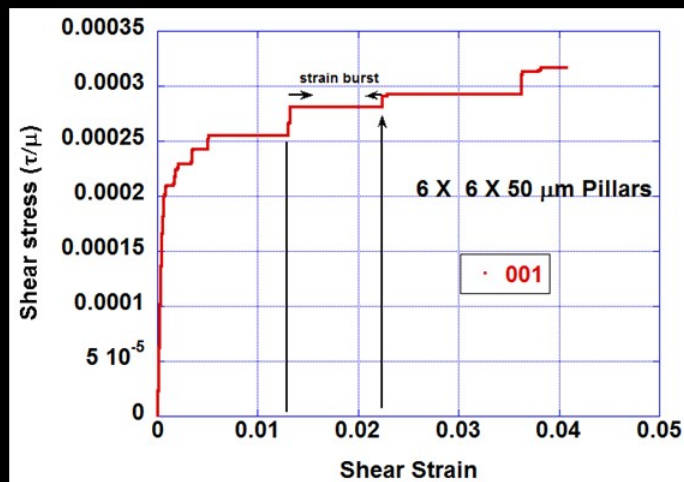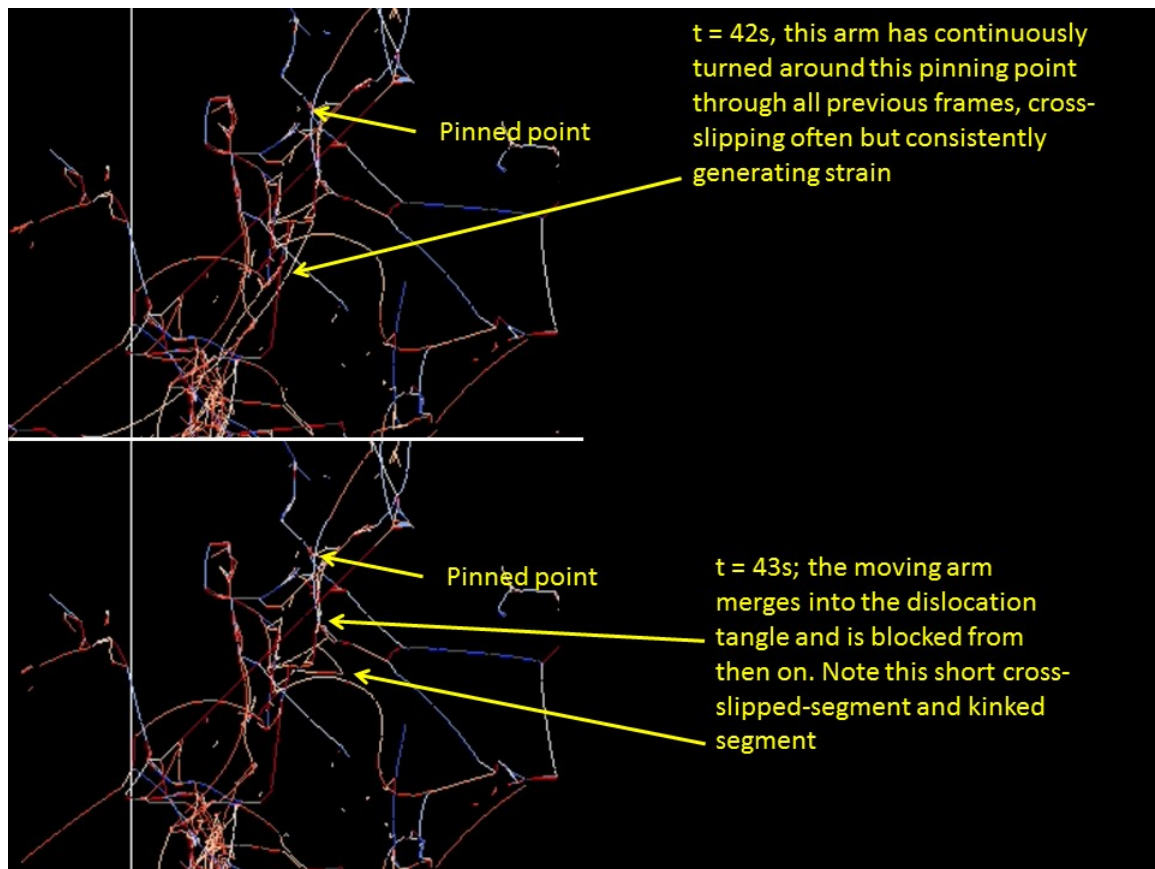
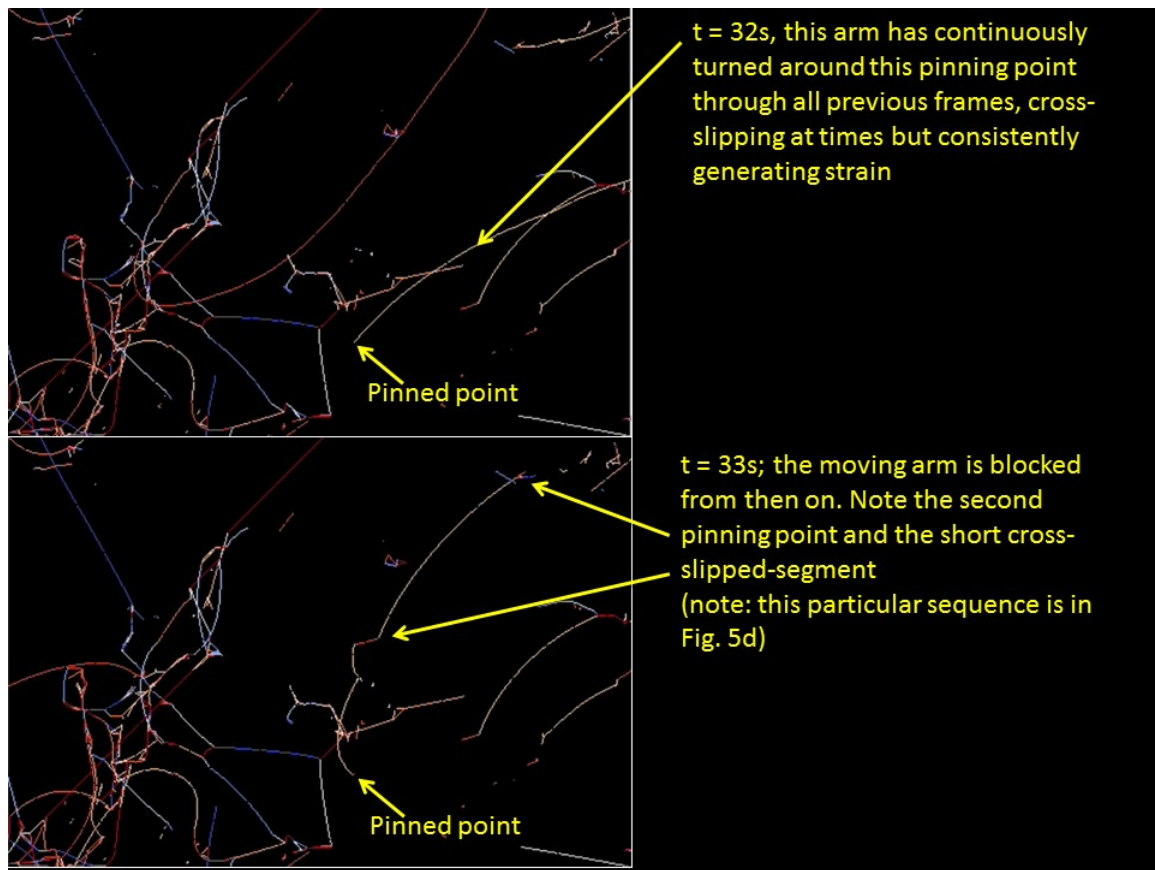Pictures in Fig. 5 are from this movie.

4.3.2 [001] movie, full cell

Dislocation microstructure evolution in a 6 × 6 × 50 µm pillar, stressed along the [001] orientation, at shear strains of 0.014 - 0.023. The whole cell and dislocations on all slip systems are shown. Note here too the continuous operation of a few single-arm sources evolved during deformation leading to the displacement burst. Also note frequent cross-slip of the single arm sources for this orientation of deformation, visible in the movie as frequent change of colors. Several sources on one side of the simulation cell cease to operate toward the middle of the movie (mechanism of cessation described in [001] part-cell movie), leading to the eventual end of the plastic displacement burst.

4.3.3 [001] movie digest

6 μm crystal oriented and deformed in tension along [001]:
Resolved stress-strain curve indicating range covered by the film

t = 23s, this arm has turned around this pinning point starting at t = 12s, cross-slipping at times but generating strain

t = 24s; the moving arm combines with the mixed plane arm here, and is blocked from then on.

t = 32s, this arm has continuously turned around this pinning point through all previous frames, cross-slipping at times but consistently generating strain

Pinned point

t = 33s; the moving arm is blocked from then on. Note the second pinning point and the short cross-slipped-segment
(note: this particular sequence is in Fig. 5d)

Pinned point

t = 42s, this arm has continuously turned around this pinning point through all previous frames, cross-slipping often but consistently generating strain

Pinned point

Pinned point

t = 43s; the moving arm merges into the dislocation tangle and is blocked from then on. Note this short cross-slipped-segment and kinked segment
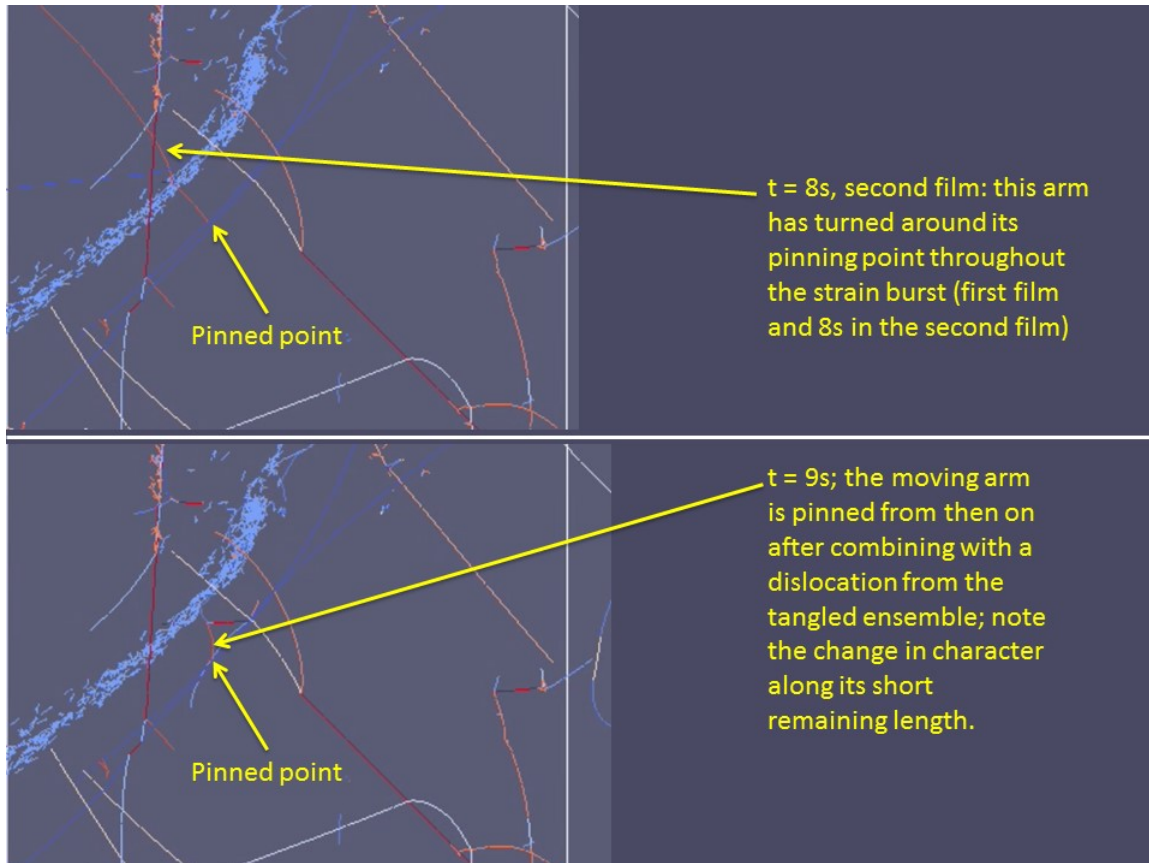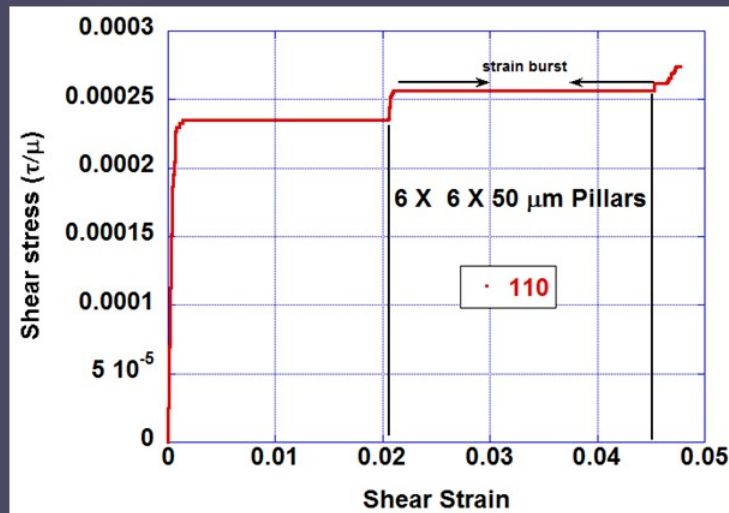
4.3.4   [110] movie, part-cell

Dislocation microstructure evolution in a 6 × 6 × 50 µm pillar, stressed along the [110] orientation, at shear strains of 0.021 - 0.045 (given in two consecutive films so as to limit the file size). Dislocations on all slip systems are shown. Note the trapping of the second slip system source (orange, (11-1)[011]) at the dislocation debris of the first slip system (light blue (111)[01-1]).

4.3.5   [110] movie, full cell

Dislocation microstructure evolution in a 6 × 6 × 50 µm pillar, stressed along the [110] orientation, at shear strains of 0.021 - 0.045 (given in two consecutive films so as to limit the file size). The whole cell and dislocations on all slip systems are shown. Note the continuous operation of a few single-arm sources evolved during deformation leading to the plastic displacement burst. One of the red sources (third source from the right in this movie Part 1) ceases to operate at the start of the Part 2 movie, leading to the eventual end of the plastic displacement burst (the mechanism of cessation is more visible in the [110] part-cell movie).

4.3.6   [110] movie digest

6 μm crystal oriented and deformed in tension along [110]:
Resolved stress-strain curve indicating range covered by the two films

t = 8s, second film: this arm has turned around its pinning point throughout the strain burst (first film and 8s in the second film)

t = 9s; the moving arm is pinned from then on after combining with a dislocation from the tangled ensemble; note the change in character along its short remaining length.

5   Microcast pure magnesium wires

In addition to aluminium, we also produced a few 99.9% purity magnesium wires with a diameter ranging from 13 μm to 15 μm. The fabrication process was identical to that used for aluminium except that, for infiltration, steel crucibles were used instead of alumina crucibles. The infiltration process was also more failure-prone with magnesium than aluminium, due to the high vapour pressure of molten magnesium (which tended for example to cause fracture of thermocouple tips).

In general the surface quality of magnesium wires was not as good as with aluminium. Many wires were covered with a rough layer, likely of magnesium oxide or hydroxide; Fig. S-16(a) gives an example. This layer probably grows either during the dissolution of the salt mould (just after dissolution, some black regions along some wires were visible in the stereomicroscope) or afterwards, while the wires were kept in a desiccator prior to testing. A few wires, however, had a relatively smooth surface; Fig. S-16(b) gives an example. We did not succeed in identifying what critical step or parameter determines whether a good or a bad surface quality is obtained with magnesium microcastings, since for all wires produced so far, the parameters of the infiltration (temperature, pressure, infiltration time) and the dissolution (time in the solution) steps in the process were all similar.
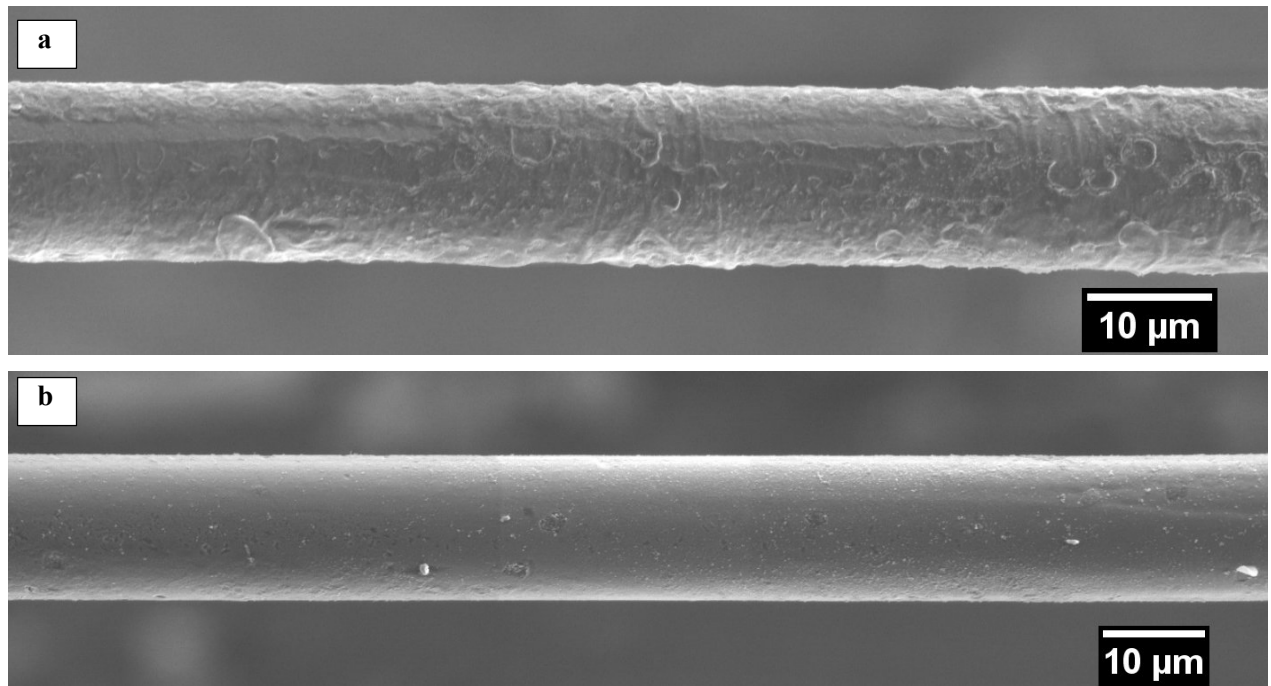
Figure S-16 - SEM images showing the rather rough surface of most of the microcast magnesium wires; likely, the roughness is linked with the formation of oxide or hydroxide along the wire surface (**a**). Image (**b**) shows one of a few wires that had a relatively smooth surface.
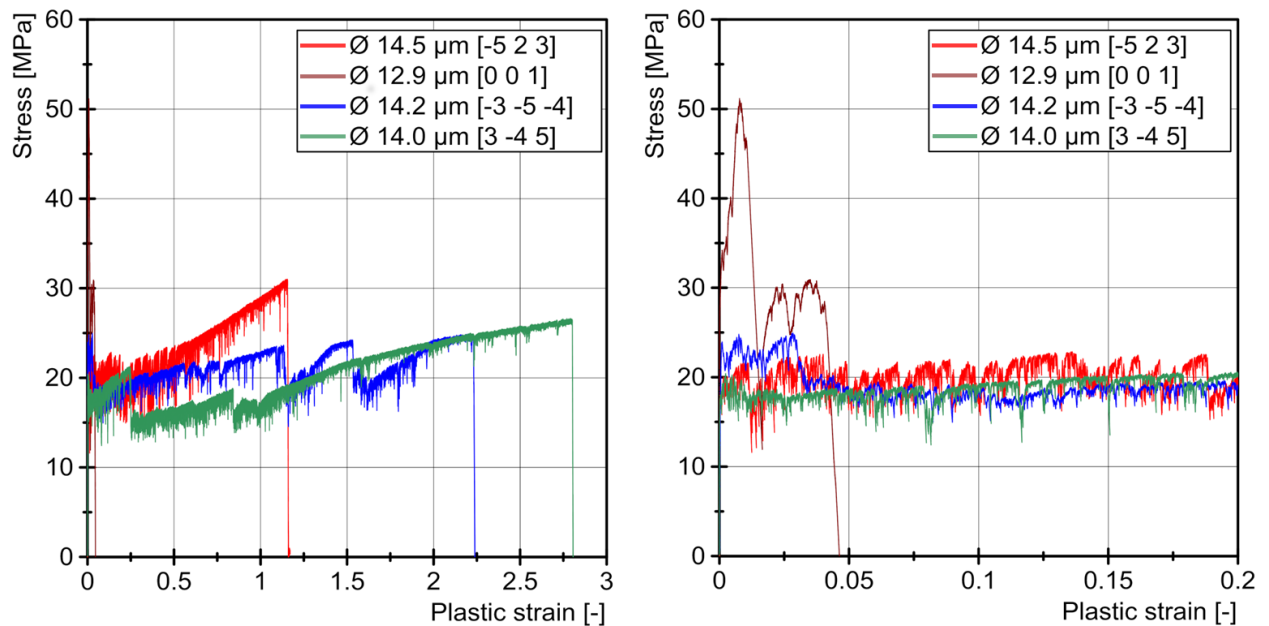

Figure S-17 - Plastic strain-stress curves of 99.9% purity magnesium wires having a diameter between 13 μm and 15 μm. (**a**) Entire whole flow curves. (**b**) A zoom on the low-strain part of (**a**) (less than 20% of plastic strain).

Magnesium wires that had a relatively smooth surface were then tested in tension following the same procedure as for aluminium wires. Their engineering tensile plastic strain-engineering stress curves are plotted in Fig. S-17. The first observation is that some flow stress curves exhibit a small stress peak in their initial part (see Fig. S-17(b)). Once plastic flow had initiated, one of two different

mechanical behaviours were observed. The wire oriented with its basal plane perpendicular to the tension axis failed directly at low strain (brown curve). Inversely, three other wires, for which the basal plane was not normal to the tensile axis, exhibited a long range of plastic deformation, with the final sample elongation exceeding 100%. Such high tensile strain ranges have already been documented for bulk HCP single crystals [S-12].

Unlike aluminium wires, where sites of plastic deformation appeared stochastically along the wire, plastic deformation in the magnesium wires took place by the propagation of a band of deformation, which started in one region and then propagated along the whole wire. Deformation of the wires by this band-propagation mechanism was associated with the appearance of many small slip lines along the deformed portion of the wires, which after testing had turned into flat ribbons, see Fig. S-18(a&b). Figure S-18(c) shows the failed region of a wire that has plastically deformed by propagation of a band going (in the figure) from its right part towards the left: this sample is interesting because fracture of the wire suddenly stopped propagation of the band, making its tip visible. In the deformed region, the rotation of the slip planes can be clearly seen as can the slip lines; however, note also the (quite spectacular) transition between the two regions: apparently, initiation of slip in the next set of basal planes is initiated by the complex three-dimensional state of stress that is created at the junction between the rotated and non-rotated portions of the single-crystal. This inhomogeneous deformation mode of pure magnesium wires oriented for basal slip makes their tensile stress-strain curves essentially meaningless, since the state of stress under which deformation is initiated and progresses is far from uniaxial stress. Curves in Fig. S-17 thus have little meaning and we have thus not analysed slip burst statistics of magnesium samples, despite the presence of strong irregularities along the stress-strain curves.

An important point that emerges from these data is that, in magnesium, once slip has initiated on the basal plane it proceeds essentially unhindered. Thus, with no cross-slip and no lock formation by interaction with dislocations on other glide systems, displacement bursts only stop for purely mechanical reasons: (i) in tensile testing because rotation of the glide plane has strongly reduced the

critical resolved shear stress or, (ii) in micropillar experiments, because the slipped region has encountered an obstacle, see Fig 2 of Ref. [S-13], or because a slipped sample portion has been fully ejected from the pillar, see Fig. 4 of Ref. [S-14]). That slip proceeds unhindered without cross-slip and lock formation is consistent with the mechanism offered here to explain how the amplitude of displacements bursts in aluminium is limited.
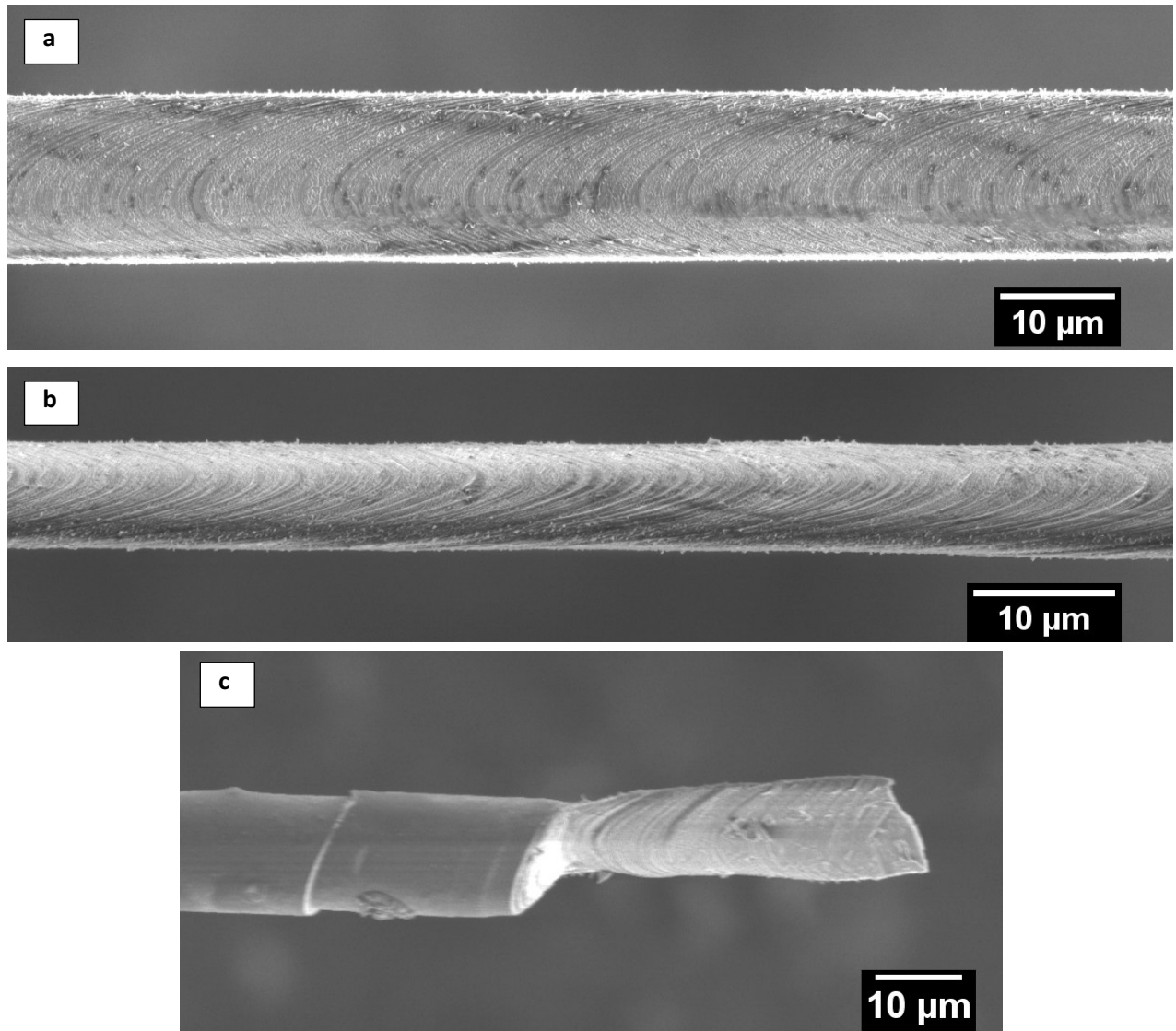

Figure S-18 - SEM images of the wire exhibiting the red flow stress curve in Fig. S-17 after deformation (**a&b**). Image (**c**) shows the failure region of another wire that had begun to deform by propagation of a plastically deformed band from right to left, and then failed before the entire wire had elongated. The extensive rotation of the glide plane can clearly be observed, as can the abruptness with which slip initiated progressively along the wire at the front tip of the propagating deformation band.

6   REFERENCES FOR SI

S-1 - Smith, S.W., *The Scientist and Engineer's Guide to Digital Signal Processing*. California Technical Publishing, San Diego, CA, USA (1997).

S-2 - Newman, M.E.J., Power laws, Pareto distributions and Zipf's law. Contemp. Phys. **46**, 323–351. (2005).

S-3 - Goodall, J.F. Despois, & A. Mortensen, "The Plasticity Size Effect in Replicated Microcellular Aluminium", Scripta Materialia, **69**, 469-472 (2013).

S-4 - Diologent, F., Goodall, R., & Mortensen, A., 2009. Surface oxide in replicated microcellular aluminium and its influence on the plasticity size effect. Acta Materialia **57**, 286–294 (2009).

S-5 - Rao, S. I., Dimiduk, D. M., Tang, M., Parthasarathy, T. A., Uchic, M. D. & Woodward, C. Estimating the strength of single-ended dislocation sources in micron-sized single crystals, Philos. Mag., **87**, 4777–4794 (2007).

S-6 - Pichaud, B., Minari, F. & Kellerhals, J. Calculation of critical shapes and stresses of surface sources of dislocations, Phil. Mag. A*., **38**, 593-602 (1978).

S-7 - Devincre, B., Kubin L.P. & Hoc, T. Physical Analyses of Crystal Plasticity by DD simulations, Scripta Materialia, **54**, 741-746 (2006).

S-8 - R. Madec, B. Devincre, L. Kubin, T. Hoc , and D. Rodney, The Role of collinear interactions in dislocation-induced hardening, Science, **301**, 1879-1882 (2003).

S-9 - Parthasarathy, T. A., Rao, S. I., Dimiduk, D. M., Uchic, M. D. & Trinkle, D. R. Contribution to size effect of yield strength from the stochastics of dislocation source lengths in finite samples, Scripta Materialia **56**, 313–316 (2007).

S-10 - Zhou, C., Beyerlein, I.R., and LeSar R., Plastic deformation mechanisms of fcc single crystals at small scales, Acta Materialia **59**, 7673-7682 (2011).

S-11 - Dimiduk, D.M., Uchic M.D., Rao, S.I., Woodward C. and Parthasarathy, T.A., Overview of experiments on microcrystal plasticity in FCC-derivative materials: selected challenges for modelling and simulation of plasticity, Modelling Simul. Mater. Sci. Eng. **15,** 135-146 (2007).

S-12 - Honeycombe, R.W., 1984. The plastic deformation of metals, Second. ed. Md.& Caulfield East : Arnold, Baltimore.

S-13 - Lilleodden, E., Micropression study of Mg (0001) single crystal, Scripta Materialia, **62**, 532-535 (2010).

S-14 – Byer C.M. and Ramesh K.T., Effects of the initial dislocation density on size effects in single-crystal magnesium, Acta Materialia, **61**, 3808-3818 (2013).